This is a preprint, the final version is subject to change, of the American Mineralogist (MSA)
Cite as Authors (Year) Title. American Mineralogist, in press.
(DOI will not work until issue is live.) DOI: http://dx.doi.org/10.2138/am-2015-5072

Revision 2

Origin and significance of the yellow cathodoluminescence (CL) of quartz

JENS GÖTZE[1,*], YUANMING PAN[2], MARION STEVENS-KALCEFF[3], ULF KEMPE[1], AND AXEL MÜLLER[4,5]

[1]TU Bergakademie Freiberg, Institute of Mineralogy, Brennhausgasse 14, 09596 Freiberg, Germany

[2]University of Saskatchewan, Department of Geological Sciences, Saskatoon, SK S7N5E2, Canada

[3]University of New South Wales, School of Physics and Electron Microscope Unit, Sydney, NSW 2052, Australia

[4] Norges Geologiske Undersøkelse, Leiv Eirikssons vei 39, N-7040 Trondheim, Norway

[5] Natural History Museum,Cromwell Road, London SW7 5BD, United Kingdom

ABSTRACT

The origin of yellow cathodoluminescence (CL) in quartz has been investigated by a combination of CL microscopy and spectroscopy, electron paramagnetic resonance (EPR) spectroscopy and spatially resolved trace-element analysis by laser ablation inductively coupled plasma-mass spectrometry (LA ICP-MS). The study shows that the appearance of a ~570 nm (2.17 eV) emission band can be attributed to high oxygen deficiency and local structural disorder in quartz. A proposed luminescence center model implies self-trapped exciton (STE) emission from localized amorphized regions in quartz. Although the high intensity emission at 570 nm is in general consistent with high concentrations of E'_1 defects detected by EPR spectroscopy, CL studies with different electron beam parameters and annealing experiments up to 600 °C show a temperature and irradiation dependence of the luminescence related defects excluding the role of

E'_1 centers as direct luminescence activators for the 570 nm emission. The evaluation of geochemical data shows that quartz with yellow CL occurs in low-temperature hydrothermal environment (mostly <250 °C) and is related to fast crystallization in an environment with oxygen deficiency.

Keywords: Cathodoluminescence (CL), yellow CL, quartz, electron paramagnetic resonance (EPR), trace elements

---

* Present address: TU Bergakademie Freiberg, Institute of Mineralogy, Brennhausgasse 14, D-09596 Freiberg, Germany. E-Mail: goetze@mineral.tu-freiberg.de

INTRODUCTION

Quartz is one of the most abundant minerals in the Earth's crust and therefore, knowledge of its specific properties is indispensable for many mineralogical and geological investigations as well as for its industrial use. The great interest in luminescence studies of quartz is due to the fact that information not available by other analytical methods can be obtained. For instance, cathodoluminescence (CL) can be used to reveal internal textures, growth zoning, secondary alteration or different quartz generations which cannot be discerned by optical or electron microscopy (e.g., Zinkernagel 1978; Ramseyer et al. 1988; Owen 1988; Ramseyer and Mullis 1990; Watt et al. 1997; Müller 2000; Götze et al. 2001a; Van den Kerkhof et al. 2004; Rusk et al. 2006, 2008; Krickl et al. 2008; Götze 2009; Müller et al. 2009, Jourdan et al. 2009a, b; Lehmann et al. 2009). In addition, CL is an effective method for spatially resolved analysis of extrinsic or intrinsic point defects in quartz by spectral measurements. The combination with electron paramagnetic resonance (EPR) spectroscopy and spatially resolved trace-element analysis provides information concerning the relation between different luminescence emission bands and specific lattice defects in the quartz structure (e.g., Stevens-Kalceff and Phillips 1995; Müller 2000; Götze et al. 2001a; Van den Kerkhof et al. 2004; Götze et al. 2005; Stevens-Kalceff 2009; Götze 2009; Götte and Ramseyer 2012).

The ideal structure of quartz is composed of SiO_4 tetrahedra, where each Si atom is surrounded by four oxygen atoms, and adjacent Si atoms are bridge-bonded through a single oxygen atom ($O_3{\equiv}Si\text{-}O\text{-}Si{\equiv}O_3$). The CL emission of quartz is in general caused by a variety of point defects including both substitutional trace elements and other lattice defects (see compilation in Stevens-Kalceff 2009; Götze 2009). The defects associated with the different CL emissions in quartz often reflect the specific physico-chemical conditions of crystal growth and therefore, can be used as a signature for genetic conditions of mineral formation (e.g., Ramseyer

et al. 1988; Müller 2000; Götze et al. 2001a; Van den Kerkhof et al. 2004; Müller et al. 2009; Götze 2009).

The most common CL emission bands in natural quartz are the 450 nm (2.75 eV) and 650 nm (1.91 eV) bands (Ramseyer et al. 1988; Götze et al. 2001a), and their nature is well known. The emission observed at ~450 nm (2.7 eV) is associated with O-deficiency centers (ODC) in quartz and is more or less identical in amorphous and crystalline SiO_2 (Imai et al. 1988; Skuja 1994, 1998; Pacchioni and Ierano 1997). The 650 nm (1.9 eV) emission is attributed to the so-called non-bridging oxygen hole center (NBOHC), which can be formed from different precursor defects (Stapelbroek et al. 1979; Siegel and Marrone, 1981; Stevens-Kalceff 2009). The common occurrence of the luminescence emissions at 450 nm (2.75 eV) and 650 nm (1.91 eV) results in bluish-violet CL colors, which are commonly detectable in quartz crystals from igneous, volcanic and metamorphic rocks, as well as authigenic quartz from sedimentary environments. In quartz from pegmatites, a characteristic transient emission around 500 nm (2.45 eV; bluish-green) is observed (Götze et al. 2004, 2005), whereas a short-lived blue CL (emission band at 390 nm – 3.18 eV) is the typical feature of natural and synthetic hydrothermal quartz (Ramseyer and Mullis 1990; Perny et al. 1992; Götze et al. 2001a). Both emissions are related to alkali-compensated trace-element centers in the quartz structure (Ramseyer and Mullis 1990; Perny et al. 1992; Gorton et al. 1996; Götze et al. 2005).

A conspicuous feature is the occurrence of yellow luminescent quartz, which is restricted to certain geological environments. In contrast to the luminescence behavior of quartz from magmatic, metamorphic and sedimentary rocks, yellow CL (~580 nm) is uncommon and was up to now detected exclusively in some natural hydrothermal quartz as well as cryptocrystalline chalcedony and agate (Rink et al. 1993; Götze et al. 1999, 2001a). There are a few reports from hydrothermal sulfide ore deposits (e.g., Moura et al. 2003; Drechsel et al. 2003; Ioannou et al. 2004) and hydrothermal gold deposits (e.g., Graupner et al. 2000; Takahashi et al. 2008; Gueye et

al. 2013), where the yellow luminescent quartz was mostly detected in late mineralization sequences. In addition, quartz with yellow CL occurs in agate, silicified wood and hydrothermal veins related to mineralization and alteration processes in volcanic rocks (Götze et al. 1999; Götze and Rößler 2000; Möckel and Götze 2007), as well as hydrothermal biomineralization (e.g. Müller et al. 2009). Sometimes, yellow luminescent quartz is associated with quartz showing transient blue CL, which is characteristic for quartz crystallized from low temperature aqueous solutions (compare Fig. 1a, k).

The observed relation of yellow luminescent quartz to specific physico-chemical environments could make this conspicuous CL feature an important genetic indicator. However, only a few suggestions concerning the origin of the yellow CL emission have been made up to now. Ramseyer et al. (1988) assumed a connection between yellow CL in quartz and elevated trace-element contents, and Müller (2000) concluded that the yellow CL in quartz may be activated by Mn^{2+} ions. Luff and Townsend (1990) measured a 570 nm emission band in Ge-doped synthetic quartz crystals at low temperature (40 K), however, they were not able to determine whether this emission can be definitively related to germanium. Other reports of yellow luminescence in natural quartz (e.g., Rink et al. 1993, Götze et al. 1999, Götze 2009) found an association with high concentrations of E'_1 defects (electron defects related to an oxygen vacancy).

The present study combines investigations by CL microscopy and spectroscopy with investigations by EPR spectroscopy and locally-resolved trace element analyses to elucidate the origin of yellow CL emission in quartz. The detailed characterization of defects involved in the activation of the CL emission comprises annealing experiments of selected quartz samples to determine the thermal stability and temperature dependent spectroscopic properties of the defect centers. The investigation of geologically well-defined samples should prove the validity of yellow luminescent quartz as an indicator for specific conditions of formation.

MATERIALS AND METHODS

Sample material

The sample material comprises quartz from different geological environments from worldwide occurrences. We focused on sample material with knowledge available on the geological background and data on the conditions of formation. The samples include quartz associated with hydrothermal ore deposits, collo-/crustiform SiO_2 from hydrothermal mineralization, silicified wood and agates from altered volcanic rocks as well as hydrothermal vein quartz. The specimens selected for the present study are compiled in Table 1. The estimated temperatures of formation in Table 1 refer to fluid inclusion or oxygen isotope studies from the cited publications.

One sample suite comprises quartz associated with different types of hydrothermal ore mineralization. The first sample (HQF) originates from late-Variscan polymetallic veins of the Freiberg district (Erzgebirge, Germany), which is situated within a metamorphic core complex (Seifert 1999). Both quartz with short-lived blue CL and yellow CL occur in the hydrothermal sulphide vein mineralization (Fig. 1a). Yellow CL is associated with primary quartz showing high abundances of CO_2-bearing fluid inclusions (Drechsel et al. 2003).

In the ~2.7 Ga Archean volcanogenic massive sulphide (VMS) mineralization of the Abitibi Greenstone belt (Canada) quartz occurs associated with ore in stockwork, veins, and interstitial fillings between lava pillows (Ioannou et al. 2003). Within the Noranda, Ben Nevis and Matagami districts, short-lived yellow CL occurs in “late” secondary hydrothermal generation of ore and stockwork quartz that crosscuts an earlier generation and infills the primary breccia porosity (sample HQN - Fig. 1b). CL revealed colloform/crustiform textures suggesting rapid silica precipitation, commonly associated with open space deposition (Ioannou et al. 2003).

In the giant Neves Corvo VMS deposit (Portugal), quartz with yellow CL is also associated with sulfide mineralization and shows irregular textures and sometimes distinct sector zoning (sample HQNC - Fig. 1c). Homogenization temperatures of more than 100 primary fluid inclusions in quartz from the Neves Corve main thrust were measured between 142 °C and 238 °C (Moura et al. 2003). Details on the Neves Corvo geology are given in Sáez et al. (1996).

Yellow luminescent quartz was found in the giant Muruntau Au quartz vein deposit (Uzbekistan), which lies in a sequence of flysch-like greenshist within the Central Kyzyl Kum sub-zone of the Southern Tien-Shan (Kotov and Poritskaya 1992). Quartz with yellow CL was detected in late secondary veinlets crosscutting the high-grade Au mineralized "central" quartz veins (sample HQMu - Fig. 1d). Fluid inclusion studies indicate the formation from H_2O-CO_2 aqueous-carbonic fluids with low salinity and temperatures between 100 and 250 °C (Graupner et al. 2000).

At the southern part of the Mátra Mts. (Hungary), in the neighborhood of Gyöngyöstarján, variable cryptocrystalline silica varieties occur together with iron mineralization in fractures and cavities of an andesite host rock (Czakó and Zelenka 1981). The genesis is related to the near surface interaction of microbial activities with an inorganic hydrothermal vent system (Müller et al. 2009). The fine-grained silica matrix, consisting of cryptocrystalline quartz with traces of moganite and opal-CT, is characterized by bright yellow CL (sample CQMa - Fig. 1e).

Another sample suite includes quartz mineralization of different origin in altered volcanic rocks. Several Permian volcanic events (288-298 Mio a) resulted in the formation of hydrothermal veins, agates and silicified wood within layers of rhyolites, ignimbrites and tuffs in the Erzgebirge basin, Germany (Schneider et al. 2005). For instance, quartz with yellow CL was found in samples of silicified wood from Chemnitz, Germany (Götze and Rößler 2000). This type of quartz was mostly detected in preserved cell structures, which were probably silicified via a non-crystalline SiO_2 precursor (sample SWCh - Fig. 1f). Yellow CL was also found in certain

agates from the acidic volcanic host rocks. The agates from St. Egidien (AStE), Hohenstein-Ernstthal (AHE) and Chemnitz (AChA), Germany occur in altered Permian ignimbrite and result probably from late- to post-volcanic alteration processes (Möckel and Götze 2007). Both banded cryptocrystalline chalcedony and macrocrystalline quartz exhibit the typical yellow CL (Fig. 1g/h). An agate sample from Gehlberg, Germany (sample AGeh) was incorporated into the sample suite for comparison, because the genesis of this agate is very similar to the material from the Erzgebirge basin. These agates formed in altered Permian volcanic rocks of the Thuringian Forest, Germany (Holzhey 1993). Despite the very similar geological background and genetic conditions of formation, chalcedony and quartz of these agates do not show the yellow CL. Fluid inclusion and oxygen isotope studies indicate a temperature of formation around 100 °C (Holzhey 1993).

Hydrothermally altered volcanic rocks from Chemnitz, Germany can also contain yellow luminescent quartz as massive vein quartz with complicated internal textures (sample QChem - Fig. 1i), sometimes showing alternating zones with transient blue and yellow CL (sample QCh - Fig. 1k).

Analytical methods

Polished thin sections were prepared for microscopic and cathodoluminescence (CL) investigations from all samples listed in Table 1. CL microscopy was carried out to document the quartz samples and to find reliable areas for spectral CL analyses. As a result of the CL studies, appropriate material for further analytical investigations was chosen.

Cathodoluminescence (CL)

CL measurements were performed on carbon-coated thin sections, first using a hot-cathode CL microscope HC1-LM (Neuser et al. 1995). The system was operated at 14 kV and 0.2

mA (~10 μA/mm^2) with a defocused electron beam. Luminescence images were captured using a Peltier cooled digital video-camera (OLYMPUS DP72). CL spectra in the wavelength range 370 to 920 nm were recorded with an Acton Research SP-2356 digital triple-grating spectrograph with a Princeton Spec-10 CCD detector that was attached to the CL microscope by a silica-glass fiber guide. CL spectra were measured under standardized conditions (wavelength calibration by a Hg-halogen lamp, spot width 30 μm, measuring time 5 s). Irradiation experiments were performed to document the behaviour of the quartz samples under electron bombardment. Samples were irradiated for 10 minutes under constant conditions (14 kV, 0.2 mA) and spectra were measured initially and after every 1 minute.

Spectral CL investigations over the spectral range 250-900 nm and monochromatic CL imaging were carried out using a Schottky FESEM with Gatan XiCLone CL imaging and spectral analysis system with a Peltier cooled Hamamatsu R943-02 high sensitivity photomultiplier (Stevens-Kalceff 2013). The CL spectra were excited using a continuous electron beam (10keV, 45 nA, defocused, ~67 μA/mm^2). In addition to the measurement of initial CL spectra, the spectra as a function of irradiation exposure up to 1000 s were analyzed.

Electron paramagnetic resonance (EPR)

Aliquots of the quartz samples were separated for analyses by electron paramagnetic resonance (EPR). The sample material was carefully crushed and hand-picked under a binocular microscope. The separated fractions were treated with distilled water to remove adhering particles and then air dried. The samples were measured first without pulverization. However, the EPR analysis of clear quartz crystals before grinding provided powder-like spectra indicating the presence of “micro-crystals”. Therefore, the measurement of single-crystal EPR spectra was not possible and further measurements were made with ~200 mg of pulverized materials for each sample.

The paramagnetic centers of quartz-powder samples were investigated by EPR spectroscopy in the X-band using a Bruker EMX spectrometer operated with a microwave frequency of ~9.63 GHz. Experimental conditions included modulation frequency of 100 kHz, modulation amplitude of 0.1 mT, microwave powers from 0.02 to 20 mW to obtain optimal conditions for different center types. The spectral resolution was ~0.146 mT for wide scans from 50 mT to 6500 mT and 0.024 mT for narrow scans from 300 mT to 350 mT.

Based on the results of CL and EPR analyses, three samples were pre-selected for further trace-element studies. In addition to the polished thin sections, 200 μm thick sections of these samples were prepared for laser ablation inductively coupled plasma mass spectrometry (LA-ICP-MS) measurements.

Trace elements

Concentrations of Li, Na, K, Rb, Ca, Sr, Mn, Zn, Fe, B, Al, Ga, Ge, Ti and P were analysed by LA-ICP-MS on a double-focusing sector field mass spectrometer ELEMENT XR from Thermo Instruments coupled with a NewWave 193-nm excimer laser probe (Flem and Müller 2012). The laser had a pulse rate of 20 Hz, a speed of 15 μm s^{-1}, a spot size of 50 μm, and energy fluence of 5 to 7 mJ cm^{-2} on the sample surface. Raster ablation was applied on an area of ca. 150 × 300 μm. The depth of ablation was ca. 50 μm. The carrier gas for transport of the ablated material to the ICP-MS was He-Ar mixture. External calibration was performed using three silicate glass reference materials produced by the National Institute of Standards and Technology, USA (NIST SRM 610, 612 and 614). In addition, the NIST SRM 1830 soda-lime float glass, the certified reference material BAM No.1 amorphous SiO_2 glass from the Federal Institute for Material Research and Testing in Germany and the Qz-Tu synthetic pure quartz monocrystal provided by Andreas Kronz from the Geowissenschaftliches Zentrum Göttingen (GZG), Germany, were used. Each measurement comprised 15 scans of each isotope, with a measurement time varying from 0.15 s/scan for K in high resolution to 0.024 s/scan of, for

example, Li in low resolution. A linear regression model, including several measurements of the different reference materials, was used to define the calibration curve for each element. For the calculation of P concentrations, the procedure of Müller et al. (2008) was applied. Ten sequential measurements on the Qz-Tu synthetic pure quartz monocrystal were used to estimate the limits of detection (LOD - 3σ of 10 measurements). The analytical error ranges within 10% of the absolute concentration of the element.

Annealing experiments

Isochronal annealing experiments of two selected quartz samples were carried out to determine the thermal stability and temperature dependent spectroscopic properties of the defect centers. For this, CL and EPR spectra were measured after isochronal annealing up to 600 °C and subsequent cooling, and were compared with the untreated counterparts. Based on the results of the first studies, the agate sample from St. Egidien (AStE) was selected for these investigations, because it consists of both microcrystalline chalcedony and macro-crystalline quartz. In addition, hydrothermal vein quartz from Chemnitz, Germany (QChem) was chosen. Both samples show the typical yellow CL but differ in chemical composition, in particular in the contents of elements which might be possible activators for CL (e.g., Al and Ge).

The annealing experiments were made in a Thermolyne muffle furnace under air following the procedure of Pan and Hu (2009). Aliquot sample pieces were isothermally annealed at 100, 150, 200, 250, 300, 400, 500, and 600 °C for 2 hours. One part of each sample was used for optical microscope cathodoluminescence (OM-CL) studies of polished thin sections including electron irradiation experiments, and the other part was used for SEM-CL and EPR measurements. SEM-CL measurements were performed first without any preparation or coating of the material using a JEOL JSM-7001F (20 kV, 2.64 nA, ca. 300 µm defocused electron beam, measurement time 40s) to enable subsequent EPR studies on the identical material.

RESULTS

Cathodoluminescence (CL)

The comparison between polarized light and CL micrographs revealed that most of the apparent homogeneous quartz crystals show a wide variety of internal textures under CL including oscillatory zoning, sector zoning or skeletal growth (compare Fig. 1).

Spectral analysis of CL emissions was performed for quartz with more or less homogeneous yellowish luminescent regions. Despite variations in intensity, all samples show a broad CL emission band centered at ca. 580 nm causing the visible yellow CL (Figs. 2 and 3). The yellow band at 580 nm in agate samples is dominant in macro-crystalline quartz and weaker in chalcedony with an additional band at 650 nm (1.91 eV). Deconvolution of the broad yellow CL emission band revealed that it consists of at least three overlapping emission bands (Fig. 2). The fitting procedure shows a main luminescence emission band at 2.17 eV (570 nm – FWHM 0.38 eV/200 nm), a second band at 1.91 eV (650 nm – non-bridging oxygen hole center NBOHC) and a weak and very broad band centered at 2.47 eV (probably consisting of more than one band). Additional CL emissions with mostly low intensity could be detected in some of the samples at 290 nm (4.27 eV), 380 nm (3.26 eV), 450 nm (2.69 eV), and 750 nm (1.65 eV).

The interaction with the electron beam resulted in significant changes of the CL emission (Fig. 3), i.e. lower intensity and a shift of the band position to longer wavelength. These changes are due to a variation in the intensity ratio of the main emission band at 570 nm (2.17 eV) and the broad 650 nm (1.91 eV) band, which behave differently under the electron beam. Figure 3 illustrates a nearly exponential decrease of the intensity of the 570 nm (2.17 eV) CL emission band. The 650 nm emission is very sensitive to electron irradiation. The increase of this emission

band during electron irradiation (especially in chalcedony) results from the transformation of precursor centers into NBOHC under the electron beam.

Monochromatic CL imaging at different wavelengths was performed to get information about the spatial distribution of the defect centers responsible for the different luminescence emissions. The images in Figure 4 reveal similar spatial distribution of the defects responsible for the 570 nm (2.17 eV) and 650 nm (1.91 eV) CL emission, respectively, whereas the spatial distribution of those associated with the 290 (4.27 eV) and 380 nm (3.26 eV) emissions are different.

Another feature is visible when comparing the distribution pattern of the 570 nm (2.17 eV) CL emission with the surface morphology of the electron-irradiated sample surface (Fig. 5). Secondary electron imaging (SEM topography image) of the sample surface of quartz (agate St. Egidien) after prolonged electron irradiation reveals visible surface expansion indicating amorphization of parts of the irradiated micro-volume (Fig. 5a). The monochromatic CL image of the same area shows that the degree of enhanced expansion/amorphization approximately anti-correlates with the 570 nm (2.17 eV) emission (Fig. 5b).

Electron paramagnetic resonance (EPR)

Figure 6a shows the spectra of five selected samples in a wide scan measured at a microwave power of 2 mW. The sample suite comprises the yellow luminescent hydrothermal quartz from Chemnitz (QChem – Fig. 1i), bluish luminescent agate from Gehlberg (AGeh – not shown in Fig. 1), hydrothermal quartz from Chemnitz with zones of blue and yellow CL (QCh – Fig. 1k), and the yellow luminescent agates from St. Egidien (AStE – Fig. 1h) and Chemnitz (AChA – not shown in Fig. 1). The EPR spectra contain a characteristic oxygen-vacancy electron center E'_1 (Mashkovtsev et al. 2013) and an orthorhombic Fe^{3+} center at the effective g value of 4.28 (Weil 1994; SivaRamaiah et al. 2011).

A closer look at the central magnetic region (Figs. 6b, 7) shows further multiple species of silicon-vacancy hole centers (e.g., superoxide and ozonide radicals such as B, B′, C and C′ - Botis et al. 2005; Pan et al. 2008, 2009) and an unknown center #3 with the effective g values of 2.008, 2.006 and 2.0045 (Mashkovtsev et al. 1978). The agate from St. Egidien (AStE) is particularly interesting in that it contains abundant B/B′ and C/C′ centers, even more than quartz samples from high-grade uranium deposits (compare Botis et al. 2005 and Pan and Hu 2009).

The effective g values of all detected signals are shown in the experimental spectrum in Figure 7, which shows spectra of separated macro-crystalline quartz and chalcedony parts of the agate from St. Egidien (AStE). The broad peak at g = 2.034 arises from superoxide centers (O_2^-) B and B', while the signal at g = 2.017 belongs to several ozonide C (and C') radicals (O_3^- - Botis et al. 2008; Nilges et al. 2008, 2009; Pan et al. 2008, 2009). The small signal at g = 2.021, which has a microwave-power dependence different from hole centers but is similar to those of *E*' centers, is most likely related to the g = 1.983 line and corresponds to a new *E*'/H center ($g_{/\!/}$ = 2.0020 and $g_{\perp}$ = 2.010) with a proton hyperfine structure ($A_{/\!/}$ = 6.4 mT and $A_{\perp}$ = 6.7 mT), which has been observed from single-crystal EPR data (Mashkovtsev pers. comm. – see ticks in Fig. 6b). The weak signals at g = 1.997 and 1.994 belong to the Ge(B) and Ge E'_1 centers (Mashkovtsev et al. 2013).

The comparison of the EPR spectra of all investigated samples shows, that E'_1 is the dominant defect center but in varying concentrations (Fig. 6a). The yellow luminescent agates from St. Egidien (AStE) and Chemnitz (AChA), as well as the hydrothermal vein quartz from Chemnitz (QChem) are characterized by elevated concentrations of the E'_1 center. In contrast, the samples without the dominating yellow CL (agate from Gehlberg – AGeh and the hydrothermal quartz QCh) contain a relatively smaller number of this oxygen-vacancy electron center. In particular the macro-crystalline quartz in the agate from St. Egidien has much more abundant oxygen-vacancy electron centers (by several orders of magnitude) than hydrothermal and

pegmatite quartz that were measured for comparison (e.g. from Minas Gerais, Brazil and Sichuan, China), and also a higher abundance of the radiation induced defects at the effective g value of 2.00 than the counterparts in chalcedony (Fig. 7).

In addition, the agate from Chemnitz (AChA) and the chalcedony part of the St. Egidien sample (AStE) both show a spectrum with high intensities of silicon-vacancy hole centers (Figs. 6b, 7), whereas the number of these centers is lower in the macro-crystalline quartz part of AStE as well as in samples AGeh and QChem. The hydrothermal quartz QCh is generally free of silicon-vacancy hole centers.

Trace elements

Trace elements were analyzed in three selected samples in order to correlate CL, EPR properties and impurity concentrations. A profile of 15 analyses crossing the chalcedony and macro-crystalline quartz banding of the agate from St. Egidien (AStE - Fig. 8) was measured using LA-ICP-MS. Likewise, the yellow luminescent hydrothermal quartz from Chemnitz (QChem – compare Fig. 1i) and the agate from Gehlberg (AGeh) with blue CL were analyzed. The results are compiled in Table 2.

The distribution of most trace elements is heterogeneous within the samples. Not only significant differences between the macro-crystalline quartz and chalcedony parts in agate samples exist, but also heterogeneities within both areas. In addition, most trace elements are present in low concentrations, often below the limit of detection for LA-ICP-MS (e.g., Ti, Mn, Sr – Table 2). Surprisingly, this is also true for most analytical spots for Al and Na (see Fig. 8). This is in contrast to earlier investigations (e.g., Heaney and Davis 1995; Götze et al. 2001b), which reported elevated concentrations of Al and Na in agates from different occurrences worldwide.

Higher element concentrations within the agate from St. Egidien (AStE) were only detected for B, Ge and Fe. In the case of Fe, this may be due to numerous micro-inclusions of

hematite, which cause the reddish color of the chalcedony bands. However, the presence of Fe in colorless, clear quartz indicates that at least some of the Fe must be incorporated in the structure. This conclusion was supported by the EPR measurements (Fig. 6a) and the existence of a weak 750 nm CL emission, which is consistent with substitutional Fe^{3+} at Si sites (Weil 1994; SivaRamaiah et al. 2011).

The high concentrations of B and Ge in the agate from St. Egidien (AStE) are remarkable and exceed even the Clarke concentration. Interestingly, the concentrations of Ge are much higher in the quartz than the chalcedony region. The contents of Ge within the yellow luminescent quartz in the St. Egidien sample are almost two orders of magnitude higher than the average Ge contents in quartz (Götze 2009).

Trace-element concentrations within the agate from Gehlberg (AGeh) and the hydrothermal vein quartz from Chemnitz (QChem) show similar trends but also differ from sample AStE (compare Table 2). The contents of B in the agate from Gehlberg are in the same range as in the AStE sample, whereas Ge and Fe contents are much lower. In contrast, the hydrothermal quartz from Chemnitz has elevated concentrations of Al and Na and comparably low concentrations of Ge and B.

Annealing experiments

Agate (sample AStE) and hydrothermal quartz (sample QChem) were selected for tempering experiments in order to test the influence of trace elements on the luminescence emission. Both samples exhibit similar initial CL spectra with a dominant yellow emission band at 570 nm (Fig. 9). During tempering, the two samples show slightly different behavior. The intensity of the yellow CL emission at 570 nm (2.17 eV) decreases during heating up to 400 °C in the macro-crystalline quartz of sample AStE, but shows a slight increase in the hydrothermal

399 quartz (sample QChem). However, these initial trends may be due to the heterogeneities of the
400 samples leading to locally varying intensities of the yellow emission band.

401 It is noteworthy that an additional blue band at ca. 450 nm (2.69 eV) is apparent above
402 300 °C in both samples (Fig. 9). The intensity of the 450 nm emission is much stronger in macro-
403 crystalline quartz of sample AStE compared with the hydrothermal vein quartz QChem. This blue
404 emission is likely to be related to oxygen deficiency centers (ODC – Skuja 1998). After
405 annealing at 600 °C (above the phase transition temperature of 573 °C between α- and β-quartz)
406 the yellow band becomes dominant and very strong in both samples. Locally resolved spectral
407 CL measurements (OM-CL) from bright yellow and weakly luminescent regions within the
408 heterogeneous samples revealed that the blue 450 nm emission band is only visible from regions
409 with low CL intensity indicating a heterogeneous distribution of the different defect types related
410 to the 570 and 450 nm emission bands, respectively (Fig. 10).

411 Electron irradiation experiments on annealed quartz with irradiation times of up to 10
412 minutes revealed significant changes of the CL spectra. In general, the 570 nm (2.17 eV)
413 emission band decreases under the electron beam, whereas the 650 nm emission (1.91 eV) is
414 stable or slightly increases (Fig. 10). The changing intensity ratio results in an apparent shift of
415 the broad band to longer wavelengths as already observed in the untreated samples (compare Fig.
416 3) and causes a change from bright yellow to reddish brown CL (Fig. 10b). The general internal
417 CL textures like growth zoning remain visible in quartz.

418 In order to correlate the CL behaviour with possible changes in the defect structure in the
419 samples, the chalcedony and quartz parts of the agate from St. Egidien (AStE) (and their annealed
420 counterparts) have been analyzed by EPR at four different microwave powers. Those depicted in
421 Figure 11 were all measured at 0.2 mW to illustrate both silicon-vacancy and oxygen-vacancy
422 defects at the magnetic fields below and above 350 mT, respectively. Although the EPR spectra
423 of the quartz and agate parts (and their thermal behavior) are more or less similar in the oxygen-

vacancy defects, chalcedony and macro-crystalline quartz differ markedly in the spectral range relating to the silicon-vacancy hole centers in the magnetic field <350 mT.

Major changes occur in the EPR spectra after annealing between 300 and 400 °C (Figs. 11, 12). It is apparent that all defects are significantly reduced after annealing above 400 °C. The silicon-vacancy hole centers were almost annealed out in both cases.

DISCUSSION

Trace elements

The results of the spectroscopic investigations show that the 570 nm (2.17 eV) band is the dominant CL emission in yellow luminescent quartz (Fig. 2). Early reports of yellow luminescence in natural quartz indicated an association with elevated contents of trace elements (Ramseyer et al. 1988; Luff and Townsend 1990; Müller 2000). Therefore, trace elements have been measured in quartz with yellow CL to provide evidence of possible correlations. However, the results of the investigation show that there is no direct relation between the 570 nm (2.17 eV) luminescence emission in quartz and relevant trace elements. One of the proposed elements (Mn – Müller 2000) can be eliminated as an activator for the yellow luminescence emission in quartz, since the analyzed concentrations are below the detection limit of LA-ICP-MS (Table 2) and no Mn-centers were detected during EPR measurements.

Aluminum is a frequent impurity element in quartz and elevated concentrations were measured in the present quartz samples (Table 2). However, spatially resolved analyses revealed that the Al distribution is very heterogeneous. In particular, the Al contents below the detection limit of the LA-ICP-MS (< 6 ppm) have been found in macro-crystalline quartz regions that show bright yellow CL. Another argument against the possible role of Al as an activator for the 570 nm (2.17 eV) emission is the well-known relation between the alkali (or hydrogen) compensated Al

defect center ($O_3{\equiv}Al\text{-}M^+\text{-}O\text{-}Si{\equiv}O_3$) and the transient blue CL emission at ~390 nm (3.3 eV) (Alonso *et al.*, 1983; Luff and Townsend, 1990; Perny *et al.*, 1992; Gorton *et al.*, 1996).

Iron is another element that has been found in elevated concentrations in the investigated quartz samples (Table 2). EPR measurements detected an orthorhombic Fe^{3+} center at the effective g value of 4.28 (Fig. 6). This $[FeO_4/M^+]^0$ defect is characterized by substitution of Fe^{3+} for Si^{4+} with charge compensation by alkali ions or protons (Stegger and Lehmann 1989; Weil 1994). However, the macro-crystalline quartz and chalcedony samples investigated in the present study do not show any correlation between chemically analyzed Fe contents, the amount of Fe^{3+} centers measured by EPR and the signal intensity of the 570 nm (2.17 eV) CL emission. Studies which suggest the Fe^{3+}-activated CL emission in quartz are rare. Pott and McNicol (1971) reported red luminescence at 705 nm in Fe-doped synthetic SiO_2 and Stevens-Kalceff (2009) related a CL emission at 750 nm to the activation by Fe^{3+}. In summary, no conclusive relation between substitutional iron and yellow CL emission in quartz was found.

The analysed Ge contents in the studied quartz samples are elevated and sometimes remarkably high compared to average Ge contents of quartz which are in the 1 ppm level (Götze et al. 2004). In macro-crystalline quartz of the agate from St. Egidien (sample AStE), Ge contents up to 95 ppm were detected (Table 2). This sample exhibits a very intensive yellow 570 nm emission (Fig. 8). Ge-related paramagnetic defects are also present in EPR spectra but are subordinate relative to the E'_1 center (Fig. 7). Two observations argue against Ge as an activator of the yellow luminescence in quartz. First, quartz samples with moderate to low Ge concentrations (e.g. hydrothermal vein quartz from Chemnitz - QChem) show intensive 570 nm CL-emission, while conversely quartz with comparable Ge concentrations (agate from Gehlberg - AGeh) exhibits no yellow CL. Second, CL spectra of Ge-implanted SiO_2 at room temperature have been reported to show a strong blue emission band at 410 nm (3.0 eV), which is therefore

not consistent with the observed yellow CL in quartz (Barfels 2001, Fitting et al. 2002). In conclusion, the role of Ge as an activator of the yellow CL in quartz is unlikely.

E'$_1$ defects

As trace elements can be excluded as activator for the yellow CL in quartz, other lattice defects have to be taken into consideration. Previous reports of yellow luminescence in natural quartz (e.g. Rink et al. 1993, Götze et al. 1999, Götze 2009) indicated an association with high concentrations of *E*'$_1$ defects. The present study confirms that high intensity yellow CL emission is consistent with a high concentration of the *E*´$_1$ defects documented from EPR measurements, and a correlation of both relative intensities was observed. Quartz samples with high concentrations of *E*'$_1$ defects show high intensities of the 570 nm (2.17 eV) emission band (Fig. 6). In addition, the *E*'$_1$ center appears to be somewhat more abundant in macro-crystalline quartz compared to chalcedony (Fig. 7). This observation correlates very well with the higher intensity of the yellow CL emission in the macro-crystalline quartz region of agates (compare Figs. 1h and 8).

Additional information about the nature of the defect centers and their relation to the CL behavior was provided by the annealing experiments and observed changes under electron irradiation. These studies are necessary, since in contrast to EPR, CL spectroscopy is unable to detect *E*'$_1$ defects directly because of the non-radiative decay (no luminescence activation) of the center (Pacchioni and Ierano 1998). Therefore, we assume that the 570 nm (2.17 eV) CL emission is not directly associated with the paramagnetic *E*' centers, but their diamagnetic precursors and/or associated defects are most likely responsible for the characteristic yellow CL.

Annealing of the quartz samples up to 600 °C results in a continuous decrease in the concentration of *E'$_1$* centers with increasing temperature (Figs. 11, 12), whereas the yellow CL remains (Figs. 9, 10). The EPR spectra show the most drastic changes (marked reduction in

intensity of the E'_1 center) after annealing at 400/500 °C (compare Fig. 12). This correlates with the appearance and a strong increase of the 450 nm luminescence band. The *E'* centers are annealed and transformed to energetically more favourable diamagnetic defects (e.g. oxygen deficiency centers – Skuja 1998) responsible for the blue CL. This would explain the extreme increase of the 450 nm CL-emission after annealing as the conversion of E'_1 centers can be related to the high temperature treatment. This is confirmed by the fact that the intensity of the 450 nm emission after tempering correlates with the relative amount of E'_1 centers in the samples at room temperature. The agate from St. Egidien (AStE) has a higher number of initial E'_1 centers and a stronger increase of the 450 nm emission during the annealing experiments compared to the hydrothermal vein quartz from Chemnitz (QChem - compare Fig. 9). This model also explains the absence of the 450 nm luminescence in the original samples. Although the quartz is highly oxygen deficient, blue luminescence has not been observed, since *E'* centers do not activate luminescence. Only after annealing and conversion of *E'* centers into luminescence-active oxygen deficiency centers, does the characteristic 450 nm emission appear.

Self-trapped exciton (STE)

The experiments discussed above indicate that the yellow CL emission in quartz is not directly related to the paramagnetic *E'* centers detected by EPR measurements, but possibly to their diamagnetic precursors or other defects related to these paramagnetic species. Additional electron irradiation experiments showed that the yellow luminescence is modified by electron bombardment. The sensitivity to the electron beam and the decay of luminescence-active centers is demonstrated by a decrease of the 570 nm (2.17 eV) band intensity during continuous electron irradiation (Fig. 3). Mathematical calculations of the decay kinetics of different luminescence active defect centers in quartz caused by electron irradiation show an analogous behaviour with a decreasing dose curve for the self-trapped exciton (STE) related CL in amorphous and crystalline SiO_2 (Barfels 2001). The characteristic broad band width of the STE related emission (0.38

522 eV/200 nm) is in accordance with the measured FWHM of the 570 nm band in the investigated
523 quartz samples. Accordingly, we conclude that the 570 nm (2.17 eV) emission is most likely to
524 be associated with the radiative recombination of self-trapped excitons (STE).

525 Self-trapped excitons (STE) in quartz can be produced by irradiation with an electron
526 beam (Fisher et al. 1990). Self-trapping occurs when the excited electron-hole pair (i.e. the
527 exciton) creates a localized distortion in the crystalline quartz lattice. A number of potential
528 candidates for exciton-defect-pairs for the SiO_2 STE have been suggested and several forms may
529 co-exist (e.g. defect pairs with the E'_1 center and interstitial oxygen or the E'_1 center and
530 NBOHC – e.g. Stevens-Kalceff 2009). The high abundance of E'_1 and NBOHC was confirmed
531 by EPR measurements. Furthermore, the 570 nm band is often accompanied by a 650 nm (1.91
532 eV) emission (NBOHC), and monochromatic CL studies indicated that defects associated with
533 the 570 and 650 nm emissions are approximately co-located (Fig. 4).

534 An observed expansion/amorphization of quartz under the electron beam approximately
535 anti-correlates with the 570 nm (2.17 eV) emission, as indicated by CL (Fig. 5). This observation
536 is consistent with the identification of the 570 nm emission as being associated with the self-
537 trapped exciton (STE). The radiative recombination leads to the restoration of (i.e. radiative
538 relaxation to) the ideal SiO_2 microstructure: The return of the SiO_2 host lattice to its defect-free
539 structure is associated with enhanced CL emission. In contrast, non-radiative recombination of
540 the STE results in radiolytic processes (Hobbs and Pascucci 1980; Hosono et al. 1998), i.e. the
541 formation of stable defects due to the decay of electronic excitations (Tsai and Griscom 1991). In
542 case of quartz, radiolysis may cause local amorphization of the irradiated area (Stevens-Kalceff
543 and Phillips 1995, Stevens-Kalceff 2013), which is visible by surface expansion (Fig. 5).

544 Strong local disorder (including the grain boundaries of the microcrystals within the clear
545 quartz crystals) and/or local amorphization may explain the observed emission of the SiO_2 STE
546 related luminescence. In general, the STE luminescence in quartz is assumed to be related to

547 higher energy emissions and only the STE luminescence in amorphous SiO_2 shows yellow
548 luminescence (Stevens-Kalceff 2009). However, high defect concentration within quartz may
549 contribute to the local disorder within the quartz structure, resulting in slight distortions of bond
550 lengths or bond angles in the vicinity of defects (Stevens-Kalceff 2009). As a result there may be
551 amorphous-SiO_2 STE contributions to the CL emission from microscopic regions with strongly
552 disordered local environment. Similar conclusions were reported by Fitting et al. (2002), who
553 observed yellow luminescence in the initial CL spectra of highly oxygen deficient silica (SiO_X
554 with $1.5<x<1.8$). These authors related the yellow luminescence to oxygen deficient centers in
555 the form of silicon fragments or small Si-rings in the SiO_2 network.

556 Extremely high defect density has been demonstrated by EPR measurements. The studied
557 quartz samples differ from "normal" hydrothermal quartz both in the presence of complex hole
558 centers and much more abundant oxygen-vacancy electron centers (up to several orders of
559 magnitude, as in the agate from St. Egidien; Fig. 7). Structural disorder is also favoured by the
560 incorporation of Fe and OH-groups, which may result in quasi-amorphous regions within the
561 quartz structure (Graetsch et al. 1987, Rykart 1989). This highly disordered structure of yellow
562 luminescent quartz is not only visible in CL microscopy (Figs. 1 and 10) but also by other
563 microscopic techniques such as Nomarski differential interference contrast microscopy (Fig. 13).
564 Optically homogeneous quartz often shows skeletal growth, sector zoning and irregular internal
565 textures. Colloform textures and banded chalcedony are frequent in cryptocrystalline quartz
566 specimens. All these features point to a rapid crystallization under non-equilibrium conditions,
567 probably from a non-crystalline precursor.

568 In natural occurrences, it can be demonstrated that specific geological environments favor
569 the formation of defects responsible for the yellow CL in quartz. The evaluation of geochemical
570 data illustrates that quartz showing yellow CL occurs in low-temperature hydrothermal
571 environment (mostly <250 °C) and low-temperature alteration processes often accompanied by

572 CO_2-rich fluids and low oxygen fugacity (compare Table 1). This type of quartz is often observed
573 in epithermal gold mineralization as well as sulfide ore deposits. In addition, agates forming
574 during the alteration of acidic volcanic rocks may show macro-crystalline quartz and chalcedony
575 with the characteristic 570 nm (2.17 eV) emission.
576
577 **IMPLICATIONS**
578
579 The origin of yellow CL in quartz has been investigated in different types of world-wide
580 quartz occurrences. Our study shows that the dominant 570 nm (2.17 eV) CL-emission in quartz
581 is related to defect centers associated with high oxygen deficiency and local structural disorder. In
582 addition, yellow CL is restricted to natural quartz/chalcedony exclusively originating from low-
583 temperature hydrothermal environment and agates from altered acidic volcanic rocks. This close
584 relationship between the yellow emission and high concentrations of defect centres as well as the
585 specific geological environments lead to the conclusion that this luminescence can be related to
586 processes of fast crystallization (probably from a non-crystalline precursor) in an oxygen
587 deficient environment. The observations concerning appearance of quartz with yellow CL as well
588 as temperature estimations from other analytical methods (e.g. fluid inclusion studies) indicate
589 temperatures of formation mostly < 250 °C. Therefore, the appearance of yellow CL is an
590 important genetic indicator for these specific physico-chemical environments.
591 The combined EPR, CL and trace-element study shows that trace elements are unlikely to
592 be direct activators for the 570 nm (2.17 eV) CL emission in quartz, although their concentrations
593 in yellow luminescent quartz could be exceptionally high (e.g. Ge contents up to 95 ppm).
594 However, it cannot be ruled out that elevated incorporation of impurity ions causes local lattice
595 distortion. This finding is especially interesting with regard to correlations of trace-element

596 contents and CL intensities in panchromatic SEM-CL investigations. Our results evidence that
597 high-intensity CL can even appear in quartz with very low trace element contents.
598
599 **Acknowledgement**: We thank M. Drechsel (Freiberg, Germany), T. Graupner (Hannover,
600 Germany), S. Ioannou (Toronto, Canada), A. Moura (Porto, Portugal), M. Polgari (Budapest,
601 Hungary), and R. Rößler (Chemnitz, Germany) for the kind allocation of sample material. M.
602 Gaft (Tel Aviv, Israel), G. Geyer, M. Hengst, and M. Magnus (Freiberg, Germany) are gratefully
603 acknowledged for their help during the analytical work and with sample preparation,
604 respectively. The Australian Microscopy & Microanalysis Research Facility at UNSW is
605 acknowledged.
606 The Reviews of Boriana Mihailova, Alfons van den Kerkhof and an anonymous reviewer
607 significantly improved the quality of the paper.
608
609
610
611
612
613
614
615
616
617
618
619
620

REFERENCES CITED

Alonso, P.J., Halliburton, L.E., Kohnke, E.E., Bossoli, R.B. (1983) X-ray induced luminescence in crystalline SiO_2. Journal of Applied Physics, 54, 5369-5375.

Barfels, T. (2001) Kathodolumineszenz amorpher und kristalliner Modifikationen von SiO_2 and GeO_2. PhD Rostock university, 168 pp.

Botis, S., Nokhrin, S.M., Pan, Y., Xu, Y., and Bonli, T. (2005) Natural radiation-induced damage in quartz. I. Correlations between cathodoluminescence colors and paramagnetic defects. Canadian Mineralogist, 43, 1565-1580.

Botis, S., Pan, Y., and Nokhrin, S.M. (2008) Natural radiation-induced damage in quartz. III. A new radical in drusy quartz from the Atabasca Basin, Saskatchewan. The Canadian Mineralogist, 46, 125-138.

Cressey, G., Henderson, C.M.B., and van der Laan, G. (1993) Use of L-edge X-ray absorption spectroscopy to characterize multiple valence states of 3d transition metals; a new probe for mineralogical and geochemical research. Physics and Chemistry of Minerals, 20, 111–119.

Czakó, T., and Zelenka, T. (1981) New data about the neotectonics of Mátra Mountains, Northern Hungary. Advances in Space Research, 1, 289-298.

Di Benedetto, F., Innocenti, M., Tesi, S., Romanelli, M., D'Acapito, F., Fornaciai, G., Montegrossi, G., and Pardi, L.A. (2010) A Fe K-edge XAS study of amethyst. Physics and Chemistry of Minerals, 37, 283–289.

Drechsel, M., Seifert, Th., and Götze, J. (2003) Comparison of quartz-types from the polymetallic sulfide veins of the Freiberg district based on cathodoluminescence investigations. In: D.G. Eliopoulos et al., eds., Mineral Exploration and Sustainable Development. Proceedings of the 7th biennial SGA meeting, p. 763-765, Millpress, Rotterdam.

646 Fisher, A.J., Hayes, W., and Stoneham, A.M. (1990) Structure of the self-trapped exciton in
647 quartz. Physical Review Letters, 64, 2667-2670.
648 Fitting, H.-J. Barfels, T., Trukhin, A.N., Schmidt, B., Gulans, A., von Czarnowski, A. (2002)
649 Cathodoluminescence of Ge^{+}, Si^{+}, and O^{+} implanted SiO_2 layers and the role of mobile
650 oxygen in defect transformation. Journal of Non-Crystalline Solids, 303, 218-231.
651 Flem, B., and Müller, A. (2012) In situ analysis of trace elements in quartz using Laser ablation
652 inductively coupled plasma mass spectrometry. In: J. Götze and R. Möckel, eds., Quartz:
653 Deposits, Mineralogy and Analytics, p. 219-236, Springer Geology, Heidelberg, New
654 York, Dordrecht, London.
655 Gorton, N.T., Walker, G., and Burley, S.D. (1996) Experimental analysis of the composite blue
656 CL emission in quartz. Journal of Luminescence, 72-74, 669-671.
657 Götte, T., and Ramseyer, K. (2012) Trace element characteristics, luminescence properties and
658 real structure of quartz. In: J. Götze and R. Möckel, eds., Quartz: Deposits, Mineralogy
659 and Analytics, p. 265-285, Springer Geology, Heidelberg New York Dordrecht, London.
660 Götze, J. (2009) Chemistry, textures and physical properties of quartz – geological interpretation
661 and technical application. Mineralogical Magazine, 73, 645-671.
662 Götze, J., and Rößler, R. (2000) Kathodolumineszenz-Untersuchungen an Kieselhölzern - I.
663 Silifizierungen aus dem versteinerten Wald von Chemnitz (Perm, Deutschland).
664 Veröffentlichungen des Museums für Naturkunde Chemnitz, 23, 35-50.
665 Götze, J., Plötze, M., Fuchs, H., and Habermann, D. (1999) Defect structure and luminescence
666 behavior of agate – results of electron paramagnetic resonance (EPR) and CL studies.
667 Mineralogical Magazine, 63, 149-163.
668 Götze, J., Plötze, M., and Habermann, D. (2001a) Origin, spectral characteristics and practical
669 applications of the cathodoluminescence (CL) of quartz: a review. Mineralogy and
670 Petrology, 71, 225-250.

671 Götze, J., Tichomirowa, M., Fuchs, H., Pilot, J., Sharp, Z.D. (2001b) Geochemistry of agates: a
672 trace element and stable isotope study. Chemical Geology, 175, 523-541.
673 Götze, J., Plötze, M., Graupner, T., Hallbauer, D.K., and Bray, C. (2004) Trace element
674 incorporation into quartz: a combined study by ICP-MS, electron spin resonance,
675 cathodoluminescence, capillary ion analysis and gas chromatography. Geochimica et
676 Cosmochimica Acta, 68, 3741-3759.
677 Götze, J., Plötze, M., and Trautmann, T. (2005) Structure and luminescence characteristics of
678 quartz from pegmatites. American Mineralogist, 90, 13-21.
679 Graetsch, H., Flörke, O.W., and Miehe, G. (1987) Structural defects in microcrystalline silica.
680 Physics and Chemistry of Minerals, 14, 249-257.
681 Graupner, T., Götze, J., Kempe, U., and Wolf, D. (2000) Cathodoluminescence imaging as a tool
682 for characterization of quartz and trapped fluid inclusions in multistage deformed
683 mesothermal Au-quartz vein deposits: A case study from the giant Muruntau Au-ore
684 deposit (Uzbekistan). Mineralogical Magazine, 64, 1007-1016.
685 Gueye, M., Van den Kerkhof, A.M., Hein, U.F., Diene, M., Mücke, A., and Siegesmund, S.
686 (2013) Structural control, fluid inclusions and cathodoluminescence studies of Birimian
687 gold-bearing quartz vein systems in the Paleoproterozoic Mako Belt, Southwestern
688 Senegal. South African Journal of Geology, 116, 199-218.
689 Heaney, P. J., and Davis, A. M. (1995): Observation and origin of self-organized textures in
690 agates. Science, 269, 1562-1565.
691 Hobbs, L.W., and Pascucci, M.R. (1980) Radiolysis and defect structure in electron-irradiated α-
692 quartz. Journal de Physique, 7, 237-242.
693 Holzhey, G. (1993) Occurrence and genesis of agates and paragenetic minerals in rhyolites from
694 Permian volcanic rocks of the Thuringian Forest (in German). PhD thesis, TU
695 Bergakademie Freiberg.

696 Hosono, H., Kawazoe, H., and Matsunami, N. (1998) Experimental evidence for Frenkel defect
697 formation in amorphous SiO_2 by electronic excitation. Physical Review Letters, 80, 317-
698 320.
699 Imai, H., Arai, K., Imagawa, H., Hosono, H., and Abe, Y. (1988) Two types of oxygen-deficient
700 centers in synthetic silica glass. Physical Reviews B, 38, 12772-12775.
701 Ioannou, S.E., Götze, J., Weiershäuser, L., Zubowski, S.M., and Spooner, E.T.C. (2003)
702 Cathodoluminescence characteristics of Archean VMS-related quartz: Noranda, Ben
703 Nevis, and Matagami districs, Abitibi Subprovince, Canada. G^3 Online Publication, 5 (2),
704 doi:10.1029/2003GC000613.
705 Jourdan, A.-L., Vennemann, T.W., Mullis, J., Ramseyer, K., and Spiers, C.J. (2009a) Evidence of
706 growth and sector zoning in hydrothermal quartz from Alpine veins. European Journal of
707 Mineralogy, 21, 219-231.
708 Jourdan, A.-L., Vennemann, T.W., Mullis, J., and Ramseyer, K. (2009b) Oxygen isotope sector
709 zoning in natural hydrothermal quartz. Mineralogical Magazine, 73, 615-632.
710 Kotov, N.V., and Poritskaya, L.G. (1992) The Muruntau gold deposit: its geologic structure
711 metasomatic mineral associations and origin. International Geological Review, 34, 77-87.
712 Krickl, R., Nasdala, L., Götze, J., Grambole, D., Wirth, R. (2008) Alpha-irradiation effects in
713 SiO_2. European Journal of Mineralogy, 20, 517-522.
714 Lehmann, K., Berger, A., Götte, T., Ramseyer, K., and Wiedenbeck, M. (2009) Growth related
715 zonations in authigenic and hydrothermal quartz characterized by SIMS-, EPMA-, SEM-
716 CL- and SEM-CC-imaging. Mineralogical Magazine, 73, 633-643.
717 Luff, B.J., and Townsend, P.D. (1990) Cathodoluminescence of synthetic quartz. Journal of
718 Physics: Condensed Matter, 2, 8089-8097.
719 Mashkovtsev, R.I., Shcherbakova, M.Ya., and Solntsev, V.P. (1978) EPR of radiation hole
720 centers in α-quartz. Trudy Instituta Geologii I Geofyziki Akademii Nauk SSSR, Sib. Otd.

(Novosibirsk: Nauka), 385, 78-86 (in Russian).

Mashkovtsev, R.I., Li, Z., Mao, M., and Pan, Y. (2013) ^{73}Ge, ^{17}O and ^{29}Si hyperfine interactions of the Ge E`$_1$ center in crystalline SiO_2. Journal of Magnetic Resonance, 233, 7-16.

Möckel, R., and Götze, J. (2007) Achate aus sächsischen Vulkaniten des Erzgebirgischen Beckens. Veröffentlichungen des Museums für Naturkunde Chemnitz, 30, 25-60.

Moura, A., Götze, J., and Borges, F.S. (2003) Preliminary results on the cathodoluminescence of quartz from the huge Neves Corvo VMS deposit (Portugal). Boletín de la Sociedad Española de Mineralogía, 26-A, 175-176.

Müller, A. (2000) Cathodoluminescence of defect structures in quartz with applications to the study of granitic rocks. PhD thesis, University Göttingen, Göttingen, 229 p.

Müller, A., Wiedenbeck, M., Flem, B., and Schiellerup, H. (2008) Refinement of phosphorus determination in quartz by LA-ICP-MS through defining new reference material values. Geostandards and Geoanalytical Research, 32, 361-376.

Müller, A., Van den Kerkhof, A.M., Behr, H.-J., Kronz, A., and Koch-Müller, M. (2009) The evolution of late-Hercynian granites and rhyolites documented by quartz – a review. Earth and Environmental Science Transactions of the Royal Society of Edinburgh, 100, 185-204.

Müller, A., Polgári, M., Gucsik, A., Nagy, Sz., Veres, M., Pál-Molnár, E., Götze, J., Cserháti, C., Németh, T., Hámor-Vidó, M. (2009) Cathodoluminescent features and Raman spectroscopy of Miocene hydrothermal biomineralization embedded in cryptocrystalline silica varieties, Central Europe, Hungary. In: A. Gucsik, editor, Micro-Raman spectroscopy and luminescence studies in the earth and planetary sciences. AIP Conference Proceedings 1163, p. 207-218, Melville, New York.

Neuser, R.D., Bruhn, F., Götze, J., Habermann, D., and Richter, D.K. (1995) Kathodolumineszenz: Methodik und Anwendung. Zentralblatt für Geologie und Paläontologie Teil I, H. 1/2, 287-306.

Nilges, M.J., Pan, Y., and Mashkovtsev, R.I. (2008) Radiation-induced defects in quartz. I. Single –crystal W-band EPR study of an electron irradiated quartz. Physics and Chemistry of Minerals, 35, 103-115.

Nilges, M.J., Pan, Y., and Mashkovtsev, R.I. (2009) Radiation-induced defects in quartz. III. EPR, ENDOR and ESEEM characterization of a peroxy radical. Physics and Chemistry of Minerals, 36, 63-71.

Owen, M.R. (1988) Radiation-damage halos in quartz. Geology, 16, 529-532.

Pacchioni, G., and Ierano, G. (1987) Computed optical absorption and photoluminescence spectra of neutral oxygen vacancies in α-quartz. Physical Review Letters, 79, 753-756.

Pacchioni, G., and Ierano, G. (1998) Optical absorption and nonradiative decay mechanism of E' centre in silica. Physical Review Letters, 81, 377-380.

Pan, Y., and Hu, B. (2009) Radiation-induced defects in quartz. IV. Thermal properties and implications. Physics and Chemistry of Minerals, 36, 421-430.

Pan, Y., Nilges, M.J., and Mashkovtsev, R.I. (2008) Radiation-induced defects in quartz. II. W-band single-crystal EPR study of natural citrine. Physics and Chemistry of Minerals, 35, 387-397.

Pan, Y., Nilges, M.J., and Mashkovtsev, R.I. (2009) Multifrequency single-crystal EPR characterization and DFT modeling of new peroxy radicals in quartz. Mineralogical Magazine, 73, 517-535.

Perny, B., Eberhardt, P., Ramseyer, K., and Mullis, J. (1992) Microdistribution of aluminium, lithium and sodium in quartz: possible causes and correlation with short-lived cathodoluminescence. American Mineralogist, 77, 534-544.

Pott, G.T., and McNicol, B.D. (1971) Spectroscopic study of the coordination and valence of Fe and Mn ions in and on the surface of aluminas and silicas. Discussions of the Faraday Society 52, 121-131.

771 Ramseyer, K., and Mullis, J. (1990) Factors influencing short-lived blue cathodoluminescence of
772 alpha quartz. American Mineralogist, 75, 791-800.
773 Ramseyer, K., Baumann, J., Matter, A., and Mullis, J. (1988) Cathodoluminescence colours of
774 alpha-quartz. Mineralogical Magazine, 52, 669-677.
775 Rink, W.J., Rendell, H., Marseglia, E.A., Luff, B.J., and Townsend, P.D. (1993)
776 Thermoluminescence spectra of igneous quartz and hydrothermal vein quartz. Physics and
777 Chemistry of Minerals, 20, 353-361.
778 Rusk, B.G., Reed, M.H., Dilles, J.H., and Kent, A.J.R. (2006) Intensity of quartz
779 cathodoluminescence and trace-element content in quartz from the porphyry copper
780 deposit at Butte, Montana. American Mineralogist, 91, 1300-1312.
781 Rusk, B.G., Lowers, H.A., and Reed, M.H. (2008) Trace elements in hydrothermal quartz:
782 Relationships to cathodoluminescent textures and insights into vein formation. Geology,
783 36, 547-550.
784 Rykart, R. (1989) Quarz-Monographie. Ott Verlag Thun, Switzerland, 462 pp.
785 Sáez, R., Almodóvar, G.R., and Pascual, E. (1996) Geological constraints on massive sulphide
786 genesis in the Iberian pyrite belt. Ore Geology Reviews, 11, 429-451.
787 Schneider, J.W., Hoth, K, Gaitzsch, B.C., Berger, H.-J., Steinborn, H., Walther, H., and Zeidler,
788 M.K. (2005) Carboniferous stratigraphy and development of the Erzgebirge Basin. East
789 Germany. Zeitschrift der deutschen Gesellschaft für Geowissenschaften, 156, 431-466.
790 Seifert, T. (1999) Relationship between late Variscan lamprophyres and hydrothermal vein
791 mineralization in the Erzgebirge. In: Stanley, C.J. et al., editors, Mineral deposits: Process
792 to Processing, p. 429-432, Balkema, Rotterdam.
793 Siegel, G.H., and Marrone, M.J. (1981) Photoluminescence in as-drawn and irradiated silica
794 optical fibers: An assessment of the role of non-bridging oxygen defect centres. Journal of
795 Non-Crystalline Solids, 45, 235-247.

SivaRamaiah, G., Lin, J.R., and Pan, Y. (2011) Electron paramagnetic resonance spectroscopy of Fe^{3+} ions in amethyst: thermodynamic potentials and magnetic susceptibility. Physics and Chemistry of Minerals, 38, 159-167.

Skuja, L. (1994) Direct singlet-to-triplet optical absorption and luminescence excitation band of the twofold-coordinated silicon center in oxygen-deficient glass. Journal of non-crystalline solids, 167, 229-238.

Skuja, L. (1998) Optically active oxygen-deficiency-related centers in amorphous silicon dioxid. Journal of Non-Crystalline Solids, 239, 16-48.

Smith, P., and Halls, C. (1993) Preliminary report on the Flintheia base-metal prospect, Nord-Trøndelag. Feltrapport of the Norges Geologiske Undersøkelse, Trondheim, Norway.

Stapelbroek, M., Griscom, D.L., Friebele, E.J., and Sigel Jr., G.H. (1979) Oxygen-associated trapped-hole centers in high-purity fused silicas. Journal of Non-Crystalline Solids, 32, 313-326.

Stegger, P., and Lehmann, G. (1989) The structure of three centers of trivalent iron in alpha-quartz. Physics and Chemistry of Minerals, 16, 401-407.

Stevens-Kalceff, M.A. (2009) Cathodoluminescence microcharacterization of point defects in α-quartz. Mineralogical Magazine, 73, 585-606.

Stevens-Kalceff, M.A. (2013) Cathodoluminescence microanalysis of silica and amorphized quartz. Mineralogy and Petrology, 107, 455-469.

Stevens-Kalceff, M.A., and Phillips, M.R. (1995) Cathodoluminescence microcharacterization of the defect structure of quartz. Physical Reviews, B 52, 3122-3134.

Takahashi, R., Müller, A., Matsueda, H., Okrugin, V. M., Ono, S., van den Kerkhof, A.M., Kronz, A., and Andreeva, E.D. (2008) Cathodoluminescence and trace element in quartz: clues to metal precipitation mechanisms at the Asachinskoe gold deposit in Kamchatka. In: Okada, H., Mawatari, S.F., Suzuki, N. and Gautam, P., editors, Origin and evolution of

natural diversity. Proceedings of the International Symposium "The origin and evolution of the natural diversity", p. 175-184, Sapporo.

Tsai, T.E., and Griscom, D.L. (1991) Experimental evidence for excitonic mechanism of defect generation in high-purity silica. Physical Review Letters, 67, 2517-2520.

Van den Kerkhof, A.M., Kronz, A., Simon, and K., Scherer, T. (2004) Fluid-controlled quartz recovery in granulite as revealed by cathodoluminescence and trace-element analysis (Bamble sector, Norway). Contributions to Mineralogy and Petrology, 146, 637-652.

Watt, G.R., Wright, P., Galloway, S., and McLean, C. (1997) Cathodoluminescence and trace element zoning in quartz phenocrysts and xenocrysts. Geochimica et Cosmochimica Acta, 61, 4337-4348.

Weil, J.A. (1994) EPR of iron centers in silicon dioxide. Applied Magnetic Resonance, 6, 1-16.

Zinkernagel, U. (1978) Cathodoluminescence of quartz and its application to sandstone petrology. Contributions to Sedimentology, 8, 1-69.

Tables

TABLE 1. Compilation of the quartz samples investigated in the present study showing the location, type of mineralization and estimated temperatures of formation (T_f)

Location		Type	T_f [°C]	Reference
Quartz associated with hydrothermal ore deposits				
Freiberg, Germany	*HQF*	Hydrothermal vein sulfide ore deposit	155-249°C primary qtz	Drechsel et al. (2003)
Noranda, Ben Nevis, Matagami (Canada)	*HQN*	Hydrothermal VMS sulfide ore deposit	100-250°C sec. qtz	Ioannou et al. (2004)
Neves Corvo, Portugal	*HQNC*	Hydrothermal VMS sulfide ore deposit	142-238°C	Moura et al. (2003)
Muruntau, Uzbekistan	*HQMu*	Hydrothermal gold deposit	100-250°C sec. qtz	Graupner et al. (2000)
Collo-/crustiform quartz				
Mátra Mountains, Hungary	*CQMa*	Hydrothermal iron biomineralization	20-150°C	Müller et al. (2009)
Silicified wood				
Chemnitz, Germany	*SWCh*	Silicified wood in altered ignimbrite	< 200°C	Götze & Rößler (2000)
Agate				
St. Egidien, Germany	*AStE*	Agate in altered ignimbrite	176-375°C	Möckel & Götze (2007)
Hohenstein-Ernstthal, Germany	*AHE*			
Chemnitz, Germany	*AChA*			
Gehlberg, Germany	*AGeh*	Agate in altered rhyolite	ca. 100°C	Holzhey (1993)
Hydrothermal vein quartz				
Chemnitz, Germany	*QCh* *QChem*	Hydrothermal vein quartz	-	present study

TABLE 2. Results of locally resolved trace-element analysis by LA-ICP-MS (in ppm) in the agate from St. Egidien (AStE) and the hydrothermal vein quartz from Chemnitz, (QChem) both showing yellow CL, as well as the agate from Gehlberg (AGeh) without yellow CL emission; analytical points for QChem and AStE are indicated in Figure 1i and Figure 8, respectively.

	Li	Na	K	Rb	Ca	B	Ga	Al	Ge	Fe	P
AStE											
A Chalcedony	0.30	-	1.2	-	53.3	< 1	0.18	-	0.5	1.9	-
B	0.30	-	149	0.97	-	25.8	0.98	162	21.2	66.9	2.2
C	0.35	-	60.2	0.31	-	45.6	0.22	< 6.0	13.2	55.4	-
D	0.59	-	60.7	0.33	-	35.7	0.12	-	20.4	61.9	-
E	0.49	-	55.1	0.43	-	41.0	0.11	-	28.9	47.8	-
F	0.39	-	51.9	0.33	9.4	29.2	0.17	< 6.0	36.3	47.7	-
G	0.49	37.9	89.2	0.58	9.7	28.7	0.38	103	31.6	154	-
H Quartz	0.47	-	33.0	0.24	-	19.2	0.12	-	68.9	12.8	-
I	0.59	-	32.0	0.15	-	8.0	0.14	-	26.8	18.7	-
J	0.51	-	37.4	0.44	-	31.3	0.12	-	93.6	14.5	-
K	0.86	-	49.2	0.32	-	23.5	0.04	-	53.5	12.4	-
L	0.89	-	61.8	0.50	-	33.4	0.16	-	94.9	11.3	5.5
M Chalcedony	1.89	67.4	168	1.50	58.3	33.3	0.81	329	22.2	48.2	-
N	1.66	101	162	1.86	62.4	34.2	0.71	366	16.4	46.9	-
O Quartz	0.98	77.4	41.1	0.45	-	36.0	0.07	-	77.4	11.5	-

Sr < 0.1 ppm; Mn < 0.5 ppm; Zn < 0.7 ppm; Ti < 1.2 ppm; (-) = not detectable

QChem										
A Chalcedony	97.5	712	460	3.70	254	4.0	0.61	4113	0.92	773	4.5
B Quartz	1.39	65.2	24.1	0.17	3.6	5.8	1.43	88.2	1.22	10.2	6.1
C	1.67	58.1	24.8	0.14	6.2	8.4	0.43	54.5	4.18	21.4	14.5
D	1.80	36.5	30.0	0.15	2.2	5.3	-	68.1	3.30	13.2	14.9

Sr < 0.1 ppm; Mn < 0.6 ppm; Zn < 1.0 ppm; Ti not detectable; (-) = not detectable

AGeh										
A Chalcedony	33.1	110	221	3.79	110	16.5	1.00	1803	5.65	53.8	6.1
B Quartz	1.51	9.1	9.5	0.17	4.7	36.4	1.11	9.9	6.48	<0.7	5.4
C	0.86	5.5	5.2	0.25	5.2	74.3	1.28	9.8	6.03	<0.7	8.6
D	0.81	9.7	6.1	0.16	1.9	26.0	1.00	9.9	5.65	<0.7	2.0

Sr < 0.1 ppm; Mn < 0.6 ppm; Zn < 1.0 ppm; Ti not detectable; (-) = not detectable

945 **Figure captions**

946

947 **Figure 1.** Quartz samples with yellow CL investigated in the present study; **a** – Primary
948 quartz from the hydrothermal vein deposit of Freiberg, Germany (sample HQF); **b**
949 – Late secondary stockwork quartz from the VMS deposit Noranda, Canada
950 (HQN); **c** – Yellow luminescent quartz with distinct sector zoning from the
951 hydrothermal sulfide ore deposit of Neves Corvo, Portugal (HQNC); **d** – Yellow
952 luminescent quartz from late secondary veinlets of the hydrothermal gold deposit
953 of Muruntau, Uzbekistan (HQMu); **e** - Cryptocrystalline quartz with agate-like
954 structure from hydrothermal iron biomineralization of the Mátras Mountains,
955 Hungary (CQMa); **f** - Silicified wood from Chemnitz, Germany (SWCh); cell
956 structures are preserved by bright yellow luminescent quartz; **g**/**h** Polarized
957 light/CL micrograph pair of an agate sample from Chemnitz, Germany (AChA);
958 note that the quartz crystals appear completely homogeneous in polarized light,
959 only CL reveals complicated internal textures; **i** – Yellow luminescent
960 hydrothermal quartz (QChem) from altered Permian volcanic rocks from
961 Chemnitz, Germany; A-D mark the analytical spots for LA-ICP-MS analyses; **k** –
962 Hydrothermal quartz crystal from altered Permian volcanics from Chemnitz,
963 Germany (QCh); the quartz exhibits both transient blue CL as well as zones with
964 yellow CL.

965

966 **FIGURE 2.** Deconvolution of the initial broad CL emission band (see inset) of yellow
967 luminescent quartz from the Mátras Mountains, Hungary (sample CQMa -
968 compare Fig 1e); the fitting procedure shows at least three emission bands: the
969 main band at 2.17 eV (570 nm), a second band at 1.91 eV (650 nm – NBOHC) and

a weak and very broad band centered at 2.47 eV (probably consisting of more than one band).

FIGURE 3. CL spectra initially and after 600 seconds of electron irradiation of hydrothermal quartz from Chemnitz, Germany (sample QChem); the inset illustrates the exponential decrease of luminescence intensity during electron bombardment.

FIGURE 4. Monochromatic CL micrographs of a selected sample area in an agate from St. Egidien, Germany (sample AStE) with quartz and chalcedony; the comparison of the images illustrates that the distribution of the defects responsible for the 570 nm and 650 nm emission, respectively, is similar, whereas those causing the 290 and 380 nm emissions show different spatial distribution.

FIGURE 5. **a** – Secondary electron image (SEM topography image) of the sample surface of quartz (agate St. Egidien – sample AStE) after extended electron irradiation; the visible surface expansion indicates amorphization of the irradiated micro-volume; **b** - CL image (570 nm monochromatic) of the same area showing that the degree of expansion is strongly anti-correlated to the CL intensity.

FIGURE 6. Powder EPR spectra of samples AChA (agate Chemnitz Altendorf), AStE (agate St. Egidien), QCh (hydrothermal vein quartz Chemnitz with blue/yellow CL), AGeh (agate Gehlberg), and QChem (hydrothermal vein quartz Chemnitz with yellow CL); **a** – wide scans measured at a microwave power of 2 mW, showing a rhombic Fe^{3+} center as well as a pronounced E'_1 center in all samples (except QCh); **b** – the central magnetic region measured at a microwave power of 0.2 mW,

995 showing multiple species of silicon-vacancy hole centers (B/B′, C/C′ and #3)
996 centers. The ticks mark the *E*'/H center with a proton hyperfine splitting of ~6.5
997 mT.
998
999 **FIGURE 7.** Powder EPR spectra of separated quartz and chalcedony parts of the agate sample
1000 from St. Egidien, Germany (AStE), measured at 0.02 mW; quartz shows a higher
1001 abundance of the E'_1 center, whereas the silicon-vacancy hole center is more
1002 pronounced in chalcedony. The effective g values of all resolved signals in the
1003 quartz spectrum are labeled and discussed in the text.
1004
1005 **FIGURE 8.** Sample of agate from St. Egidien, Germany (AStE) with bands of chalcedony and
1006 quartz used for locally resolved trace-element analysis by ICP-MS; the dots mark
1007 the analytical points (compare results in Table 2); the inset on the left shows the
1008 CL properties of the sample area.
1009
1010 **FIGURE 9.** SEM-CL spectra on separated parts of quartz from sample AStE (**a**) and
1011 hydrothermal quartz QChem (**b**); spectra were taken on original sample pieces (20
1012 °C) and pieces after 2 h annealing at 100, 200, 300, 400, 500, and 600 °C; because
1013 of the different intensities, the spectra of the 500 and 600 °C annealed quartz in (a)
1014 are given within the inset. In both samples AStE and QChem the development of
1015 the blue CL band at 450 nm is clearly visible at temperatures above 300 °C.
1016
1017 **FIGURE 10.** OM-CL images and spectra, respectively of annealed (2h at 600 °C) sample
1018 QChem.

a/b – CL image initially (a) and after 600s of electron irradiation (b); the visible CL turns from bright yellow to reddish-brown, although the principle internal textures are still visible after electron bombardment; **c** – comparison of CL spectra from a bright yellow region (1) and a dark luminescent region (2) within the heterogeneous sample; the blue 450 nm emission band is only visible in the dark part indicating a heterogeneous distribution of the different defect types related to the 570 and 450 nm emission bands; **d** – CL spectra initially and after 600s of electron irradiation (compare a/b); the inset shows the drastic decrease of the CL intensity of the 570 nm emission band.

FIGURE 11. Comparison of powder EPR spectra, measured at a microwave power of 0.2 mW, of – **a** – quartz and – **b** – chalcedony of sample AStE as a function of annealing temperature up to 600°C; note that an isotropic signal at g = 2.003 (marked by an arrow) is visible in chalcedony but absent in quartz after annealing to 600 °C .

FIGURE 12. Intensity variations of the E'_1 center in quartz and chalcedony parts of sample AStE with annealing temperature.

FIGURE 13. Nomarski DIC micrograph of the interface chalcedony/quartz in sample AStE; skeletal growth and irregular internal textures of quartz point to rapid crystallization under non-equilibrium conditions, probably from a non-crystalline precursor.

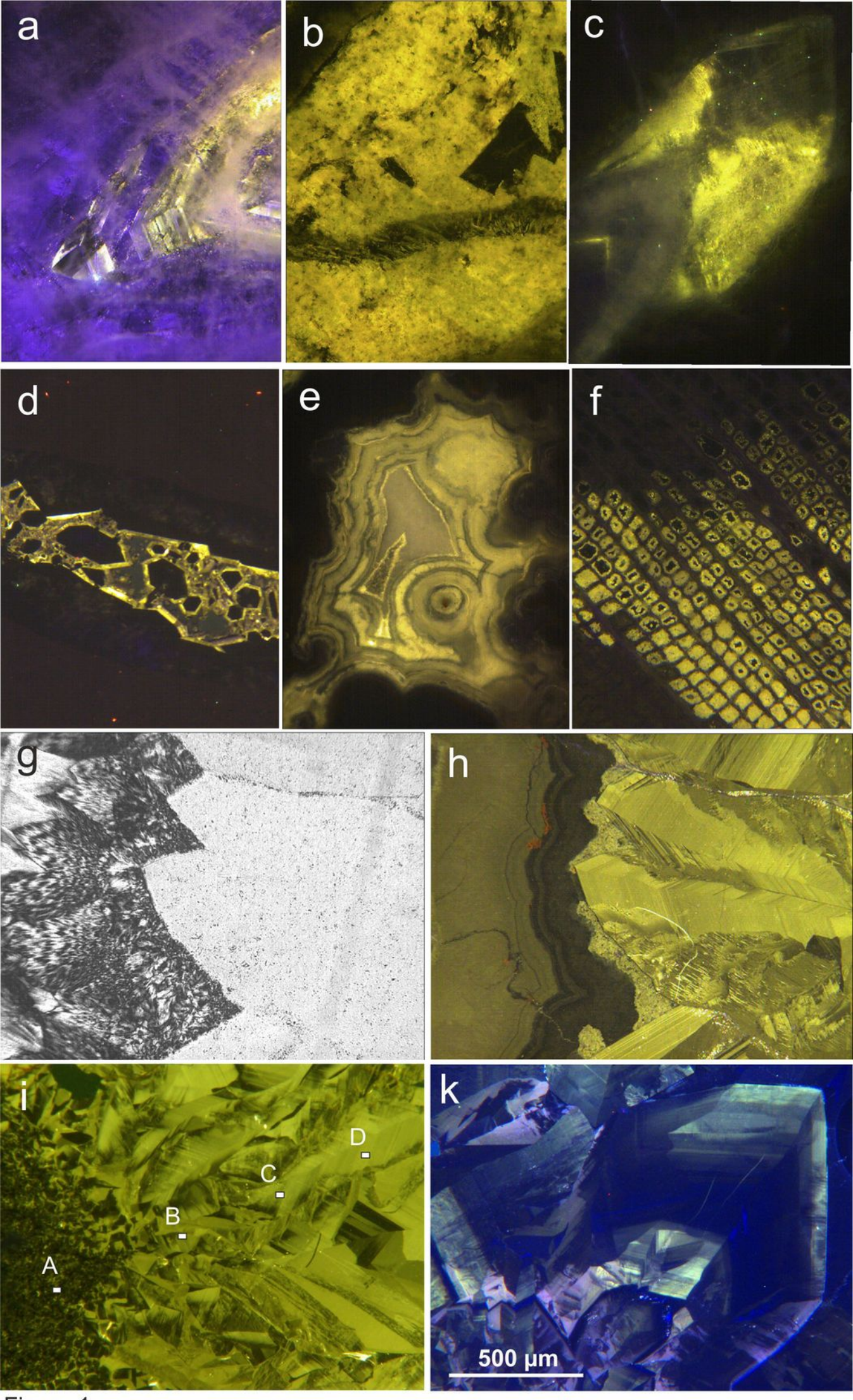

Figure 1

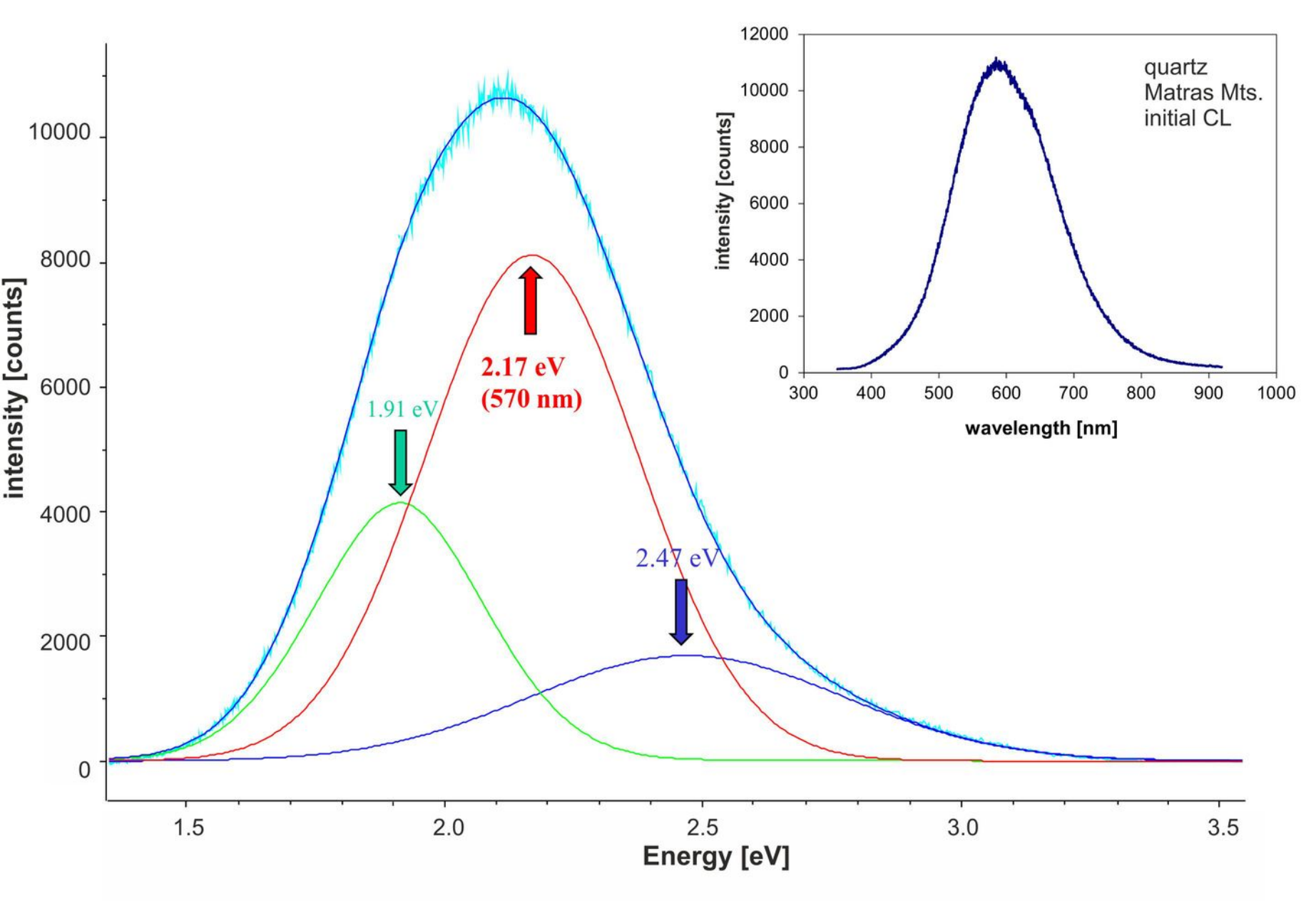
intensity [counts]
Energy [eV]
1.91 eV
2.17 eV
(570 nm)
2.47 eV
quartz
Matras Mts.
initial CL
intensity [counts]
wavelength [nm]

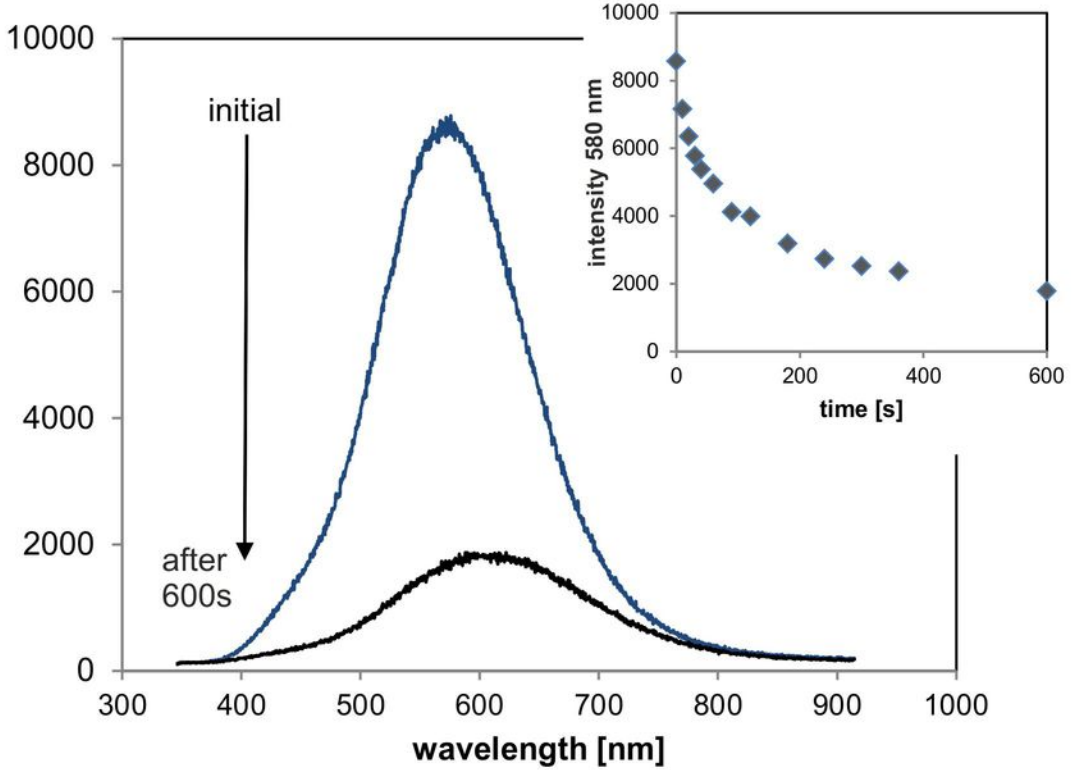
10000
8000
6000
4000
2000
0
initial
after
600s
300
400
500
600
700
800
900
1000
wavelength [nm]
intensity 580 nm
time [s]
0
200
400
600

Figure 3

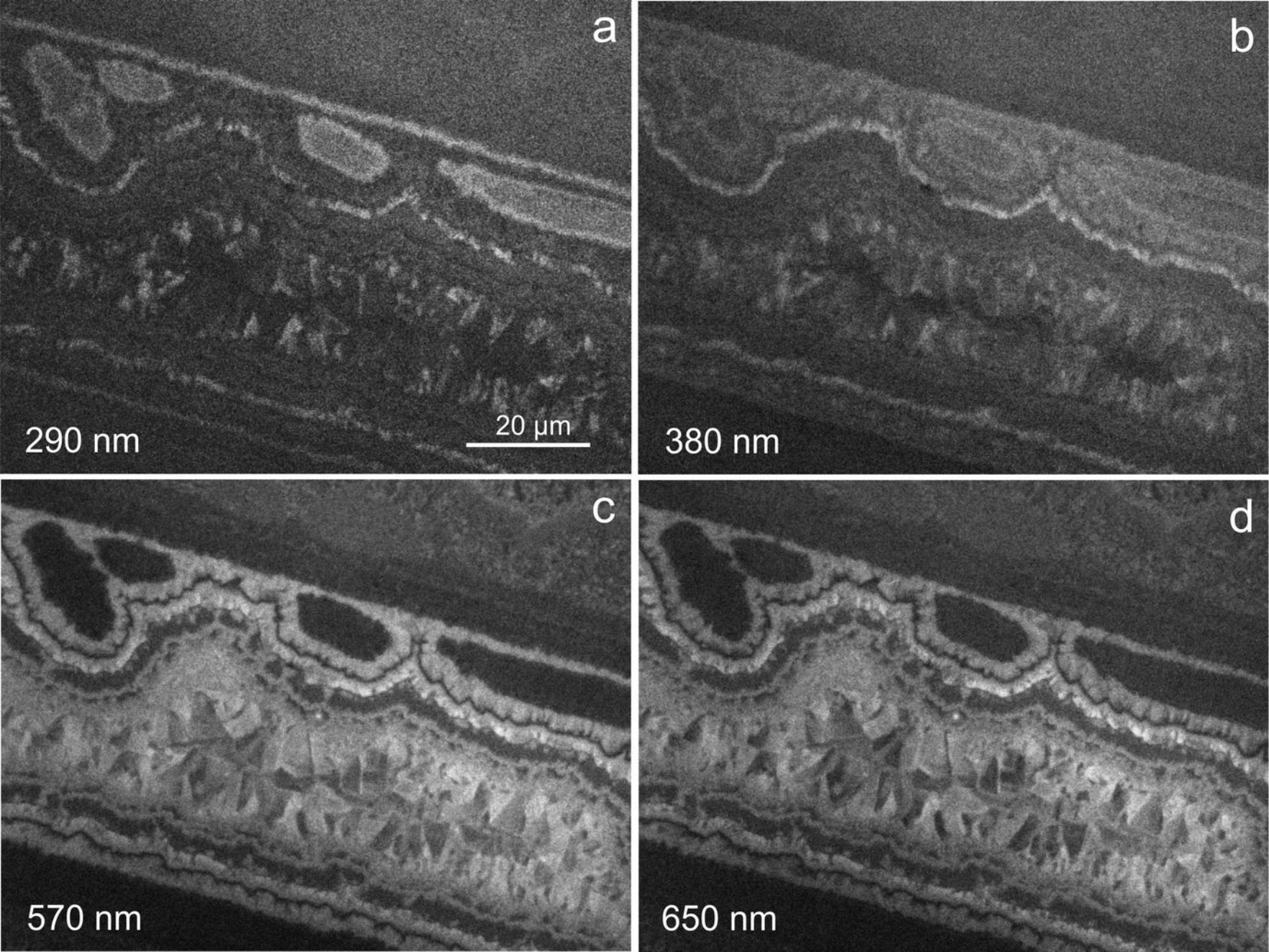
a
290 nm
20 µm
b
380 nm
c
570 nm
d
650 nm

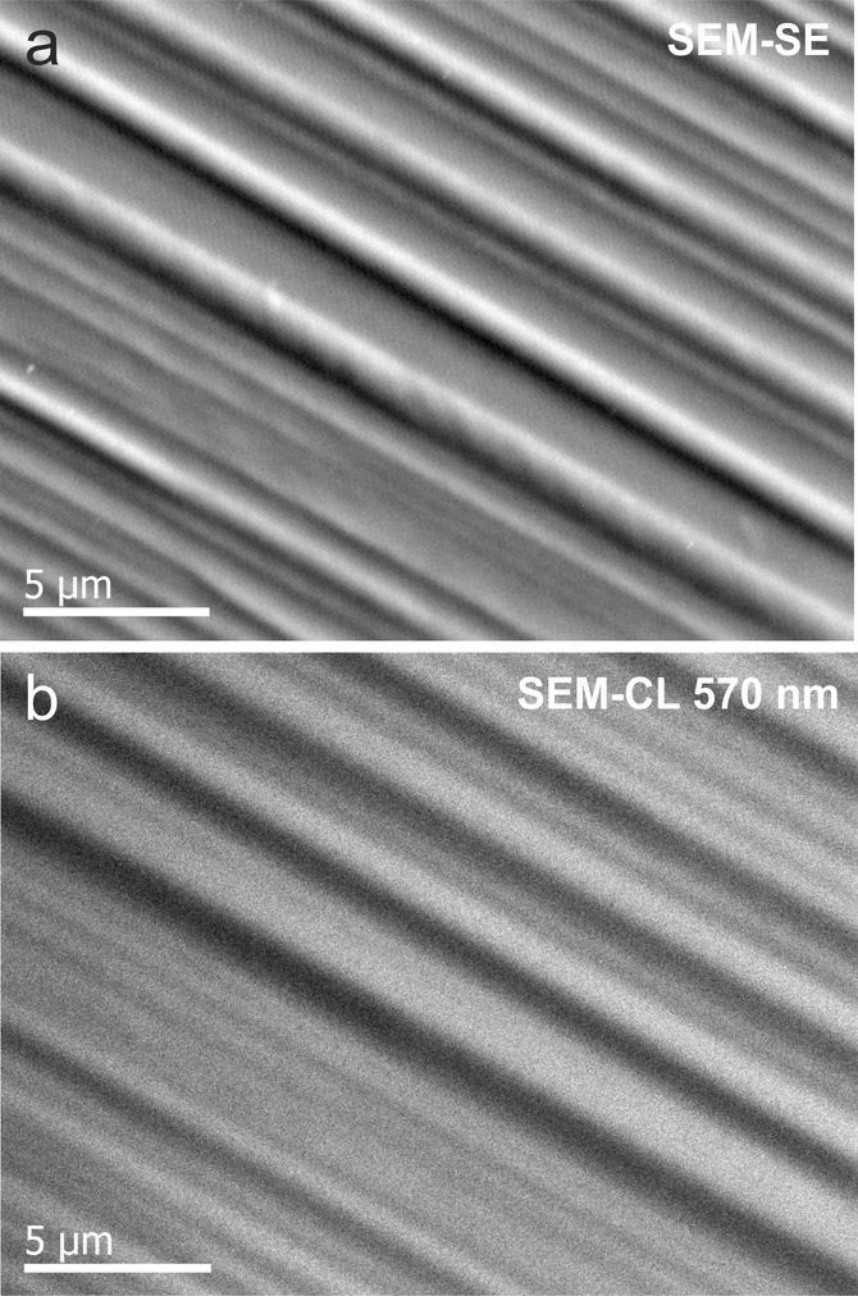
a
SEM-SE
5 µm
b
SEM-CL 570 nm
5 µm

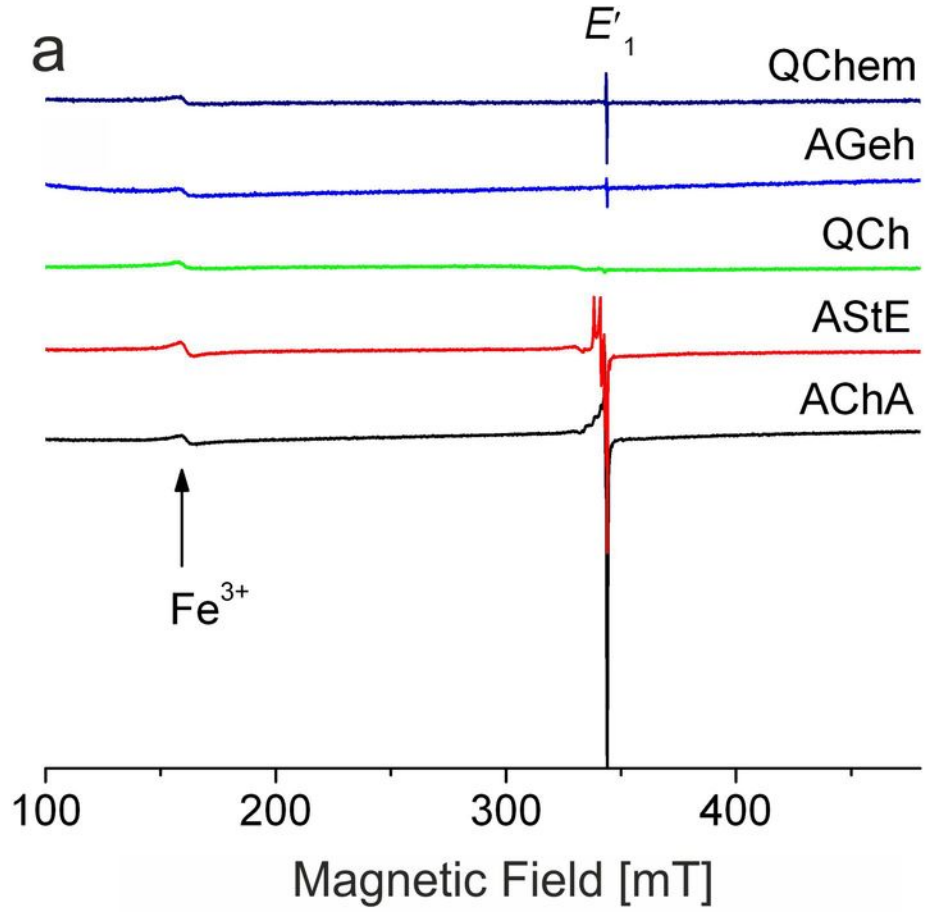
a
E′1
QChem
AGeh
QCh
AStE
AChA
Fe3+
100
200
300
400
Magnetic Field [mT]

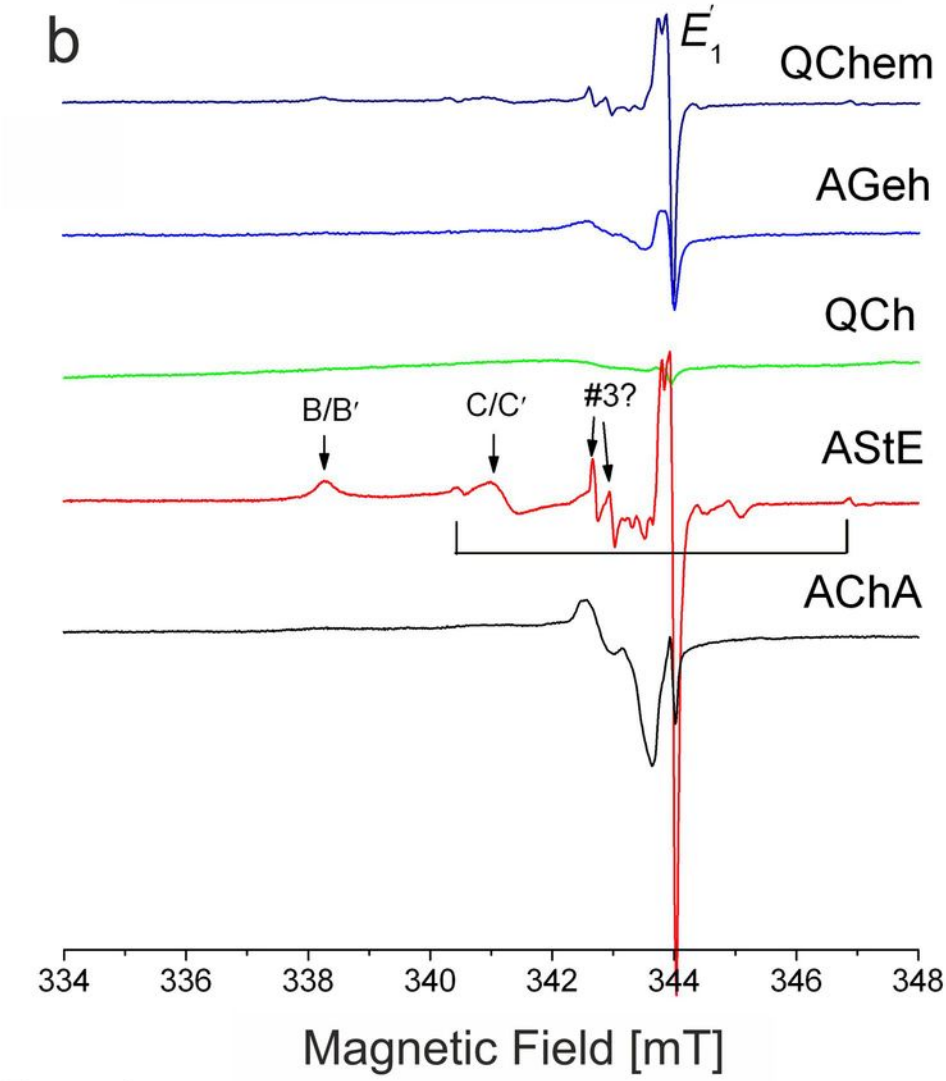
b
E′1
QChem
AGeh
QCh
B/B′
C/C′
#3?
AStE
AChA
334
336
338
340
342
344
346
348
Magnetic Field [mT]

Figure 6

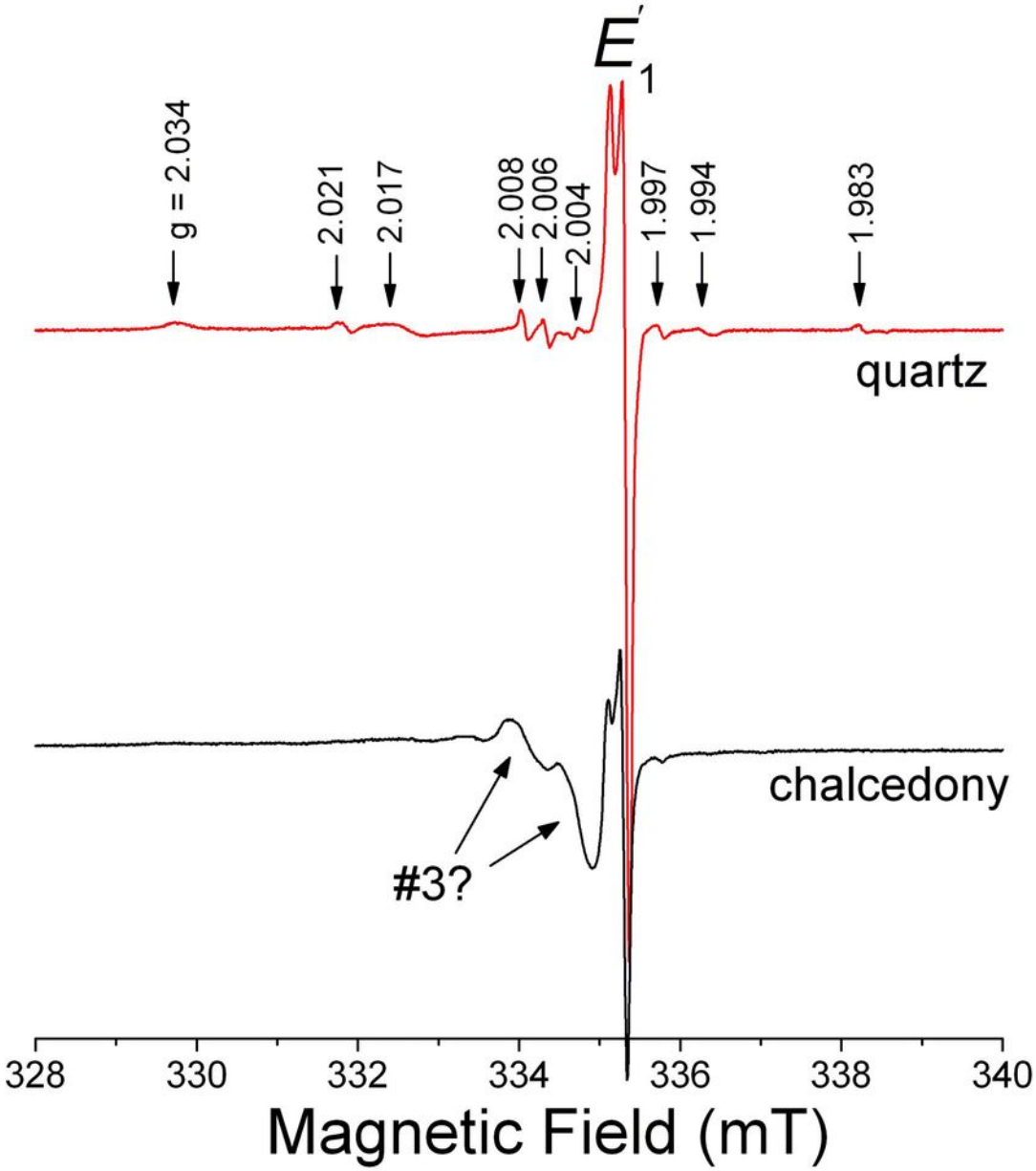
E'1
g = 2.034
2.021
2.017
2.008
2.006
2.004
1.997
1.994
1.983
quartz
chalcedony
#3?
328
330
332
334
336
338
340
Magnetic Field (mT)

Figure 7

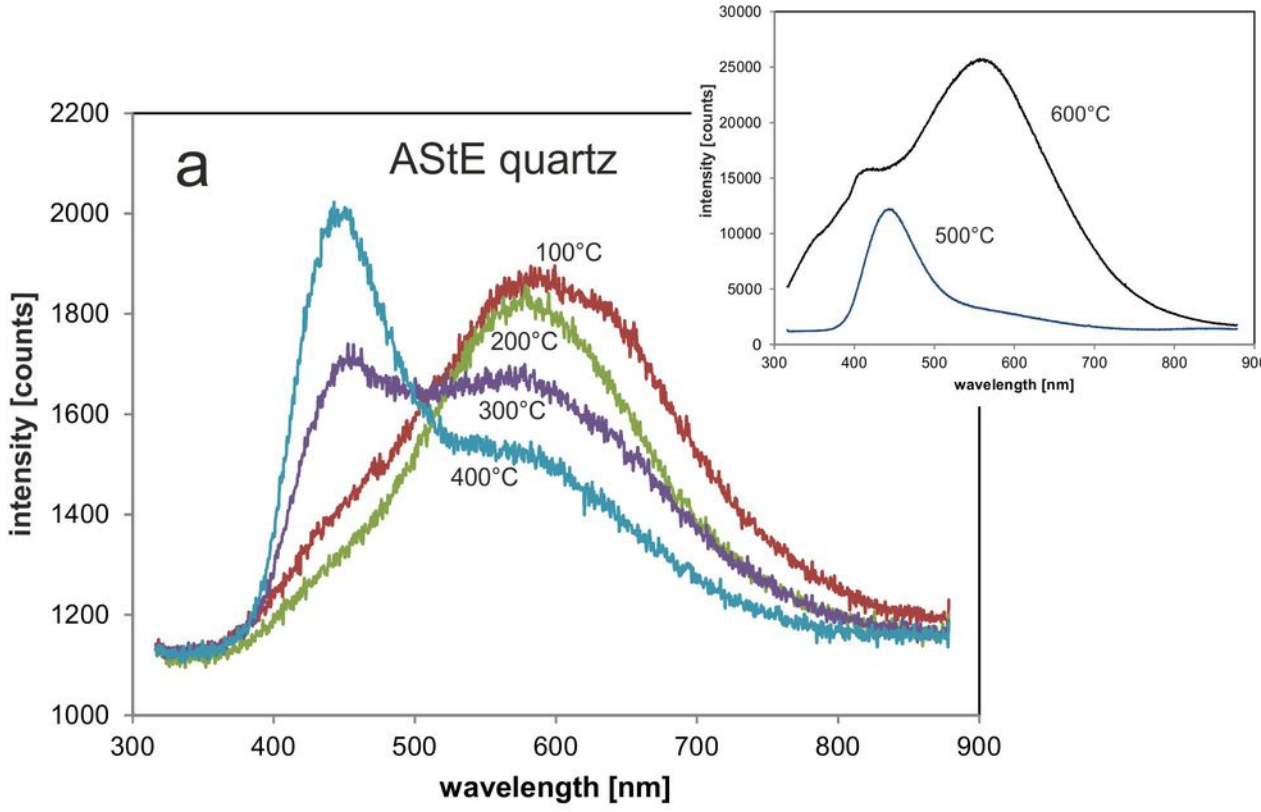
a
AStE quartz
100°C
200°C
300°C
400°C
intensity [counts]
wavelength [nm]
600°C
500°C
intensity [counts]
wavelength [nm]

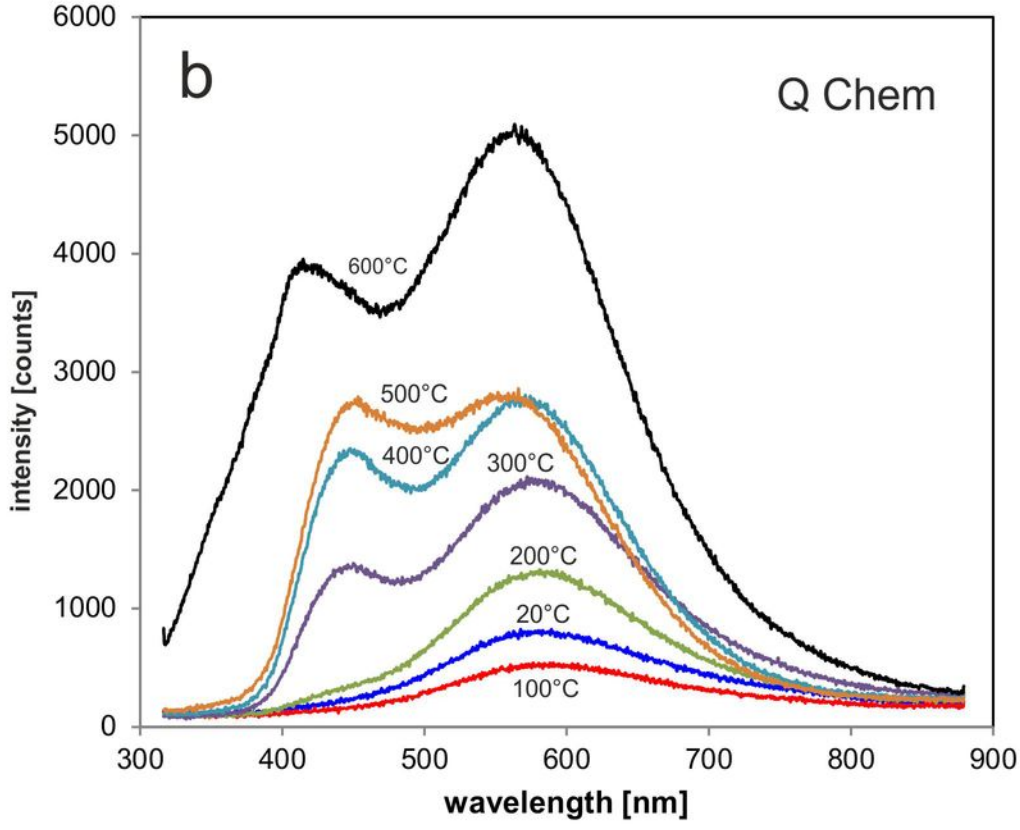
b
Q Chem
600°C
500°C
400°C
300°C
200°C
20°C
100°C
intensity [counts]
wavelength [nm]

Figure 8

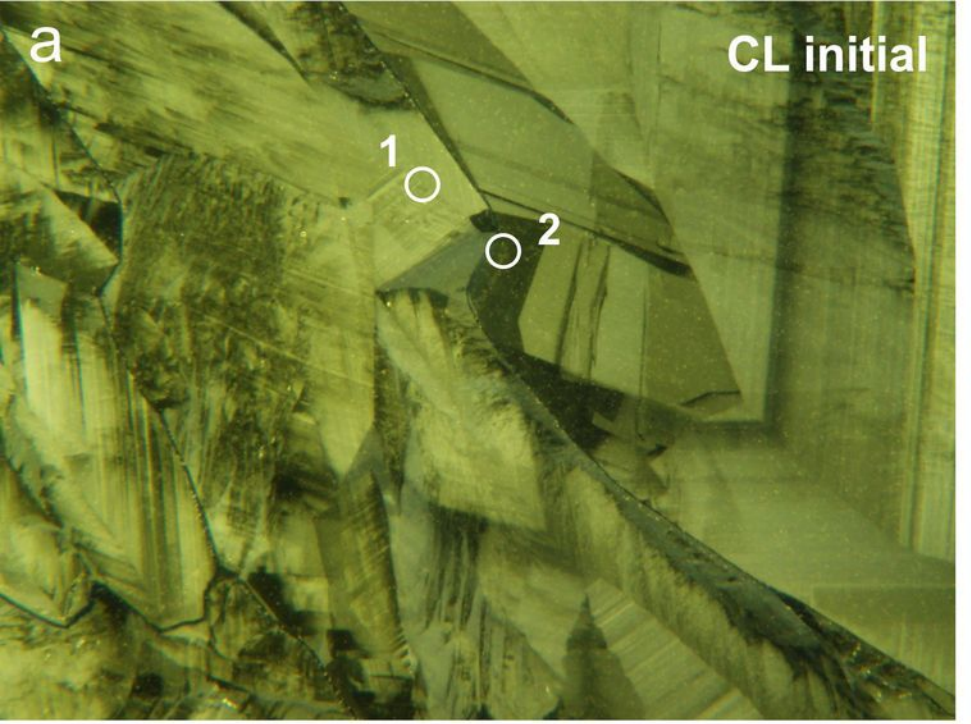
a
CL initial
1
2

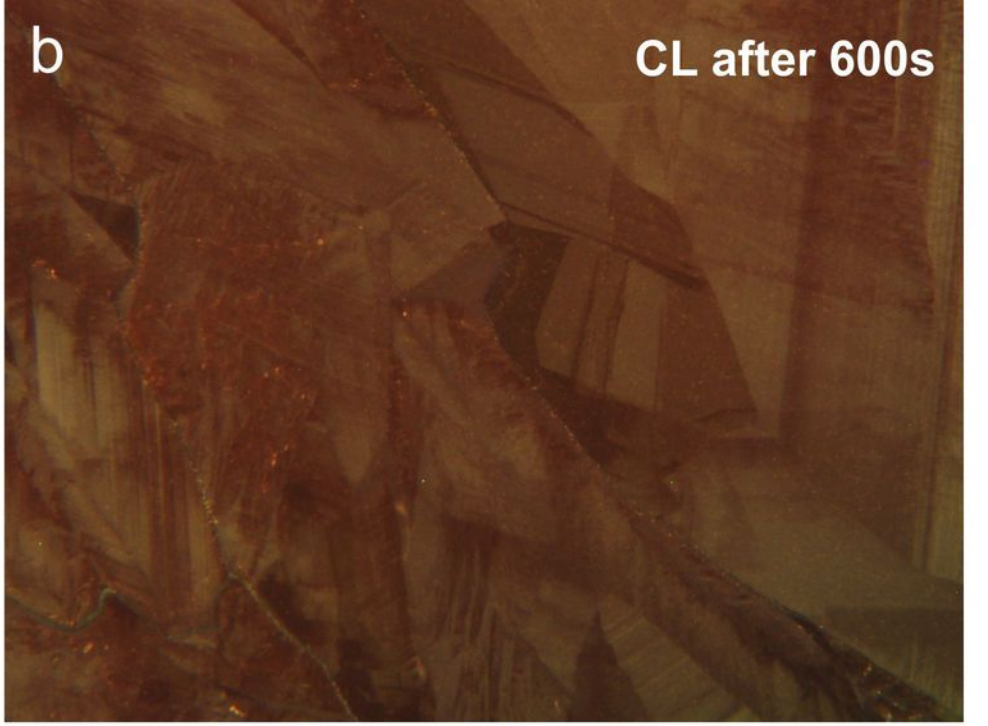
b
CL after 600s

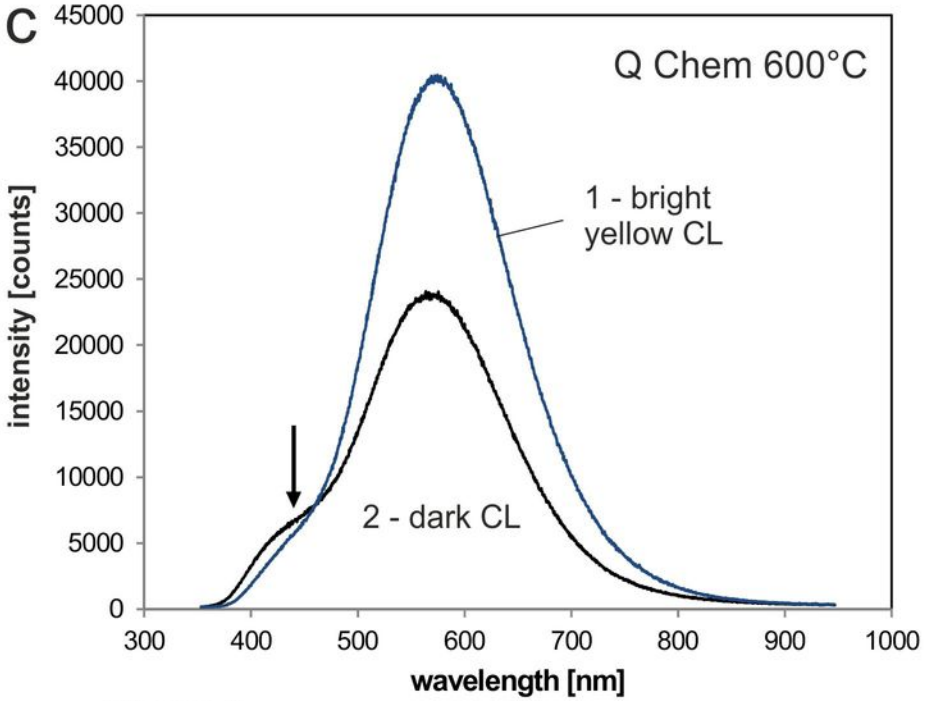
c
Q Chem 600°C
1 - bright yellow CL
2 - dark CL
intensity [counts]
wavelength [nm]
0
5000
10000
15000
20000
25000
30000
35000
40000
45000
300
400
500
600
700
800
900
1000

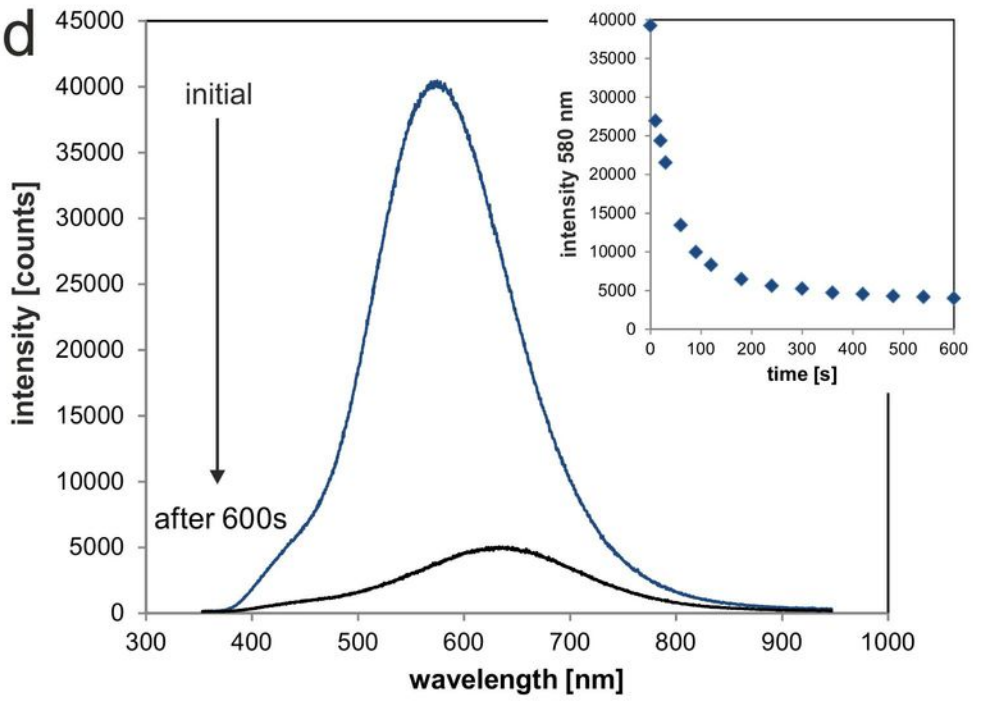
d
initial
after 600s
intensity [counts]
wavelength [nm]
intensity 580 nm
time [s]
0
5000
10000
15000
20000
25000
30000
35000
40000
45000
300
400
500
600
700
800
900
1000
0
100
200
300
400
500
600

Figure 9

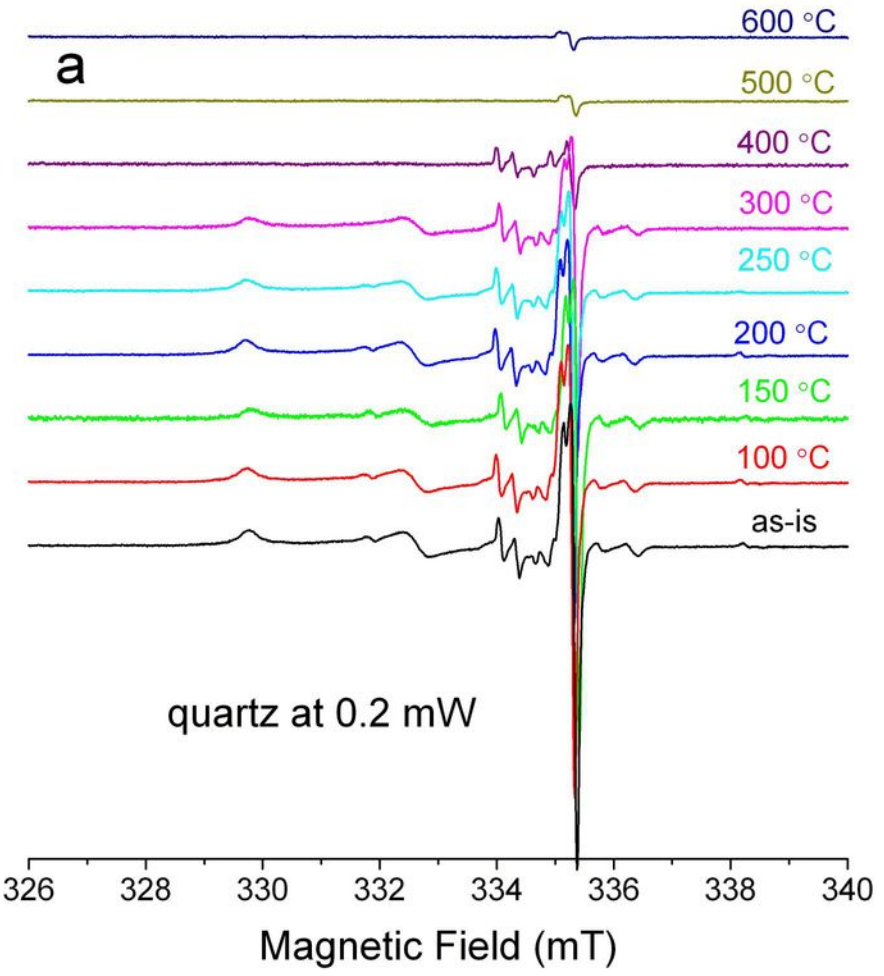
a
600 °C
500 °C
400 °C
300 °C
250 °C
200 °C
150 °C
100 °C
as-is
quartz at 0.2 mW
326
328
330
332
334
336
338
340
Magnetic Field (mT)

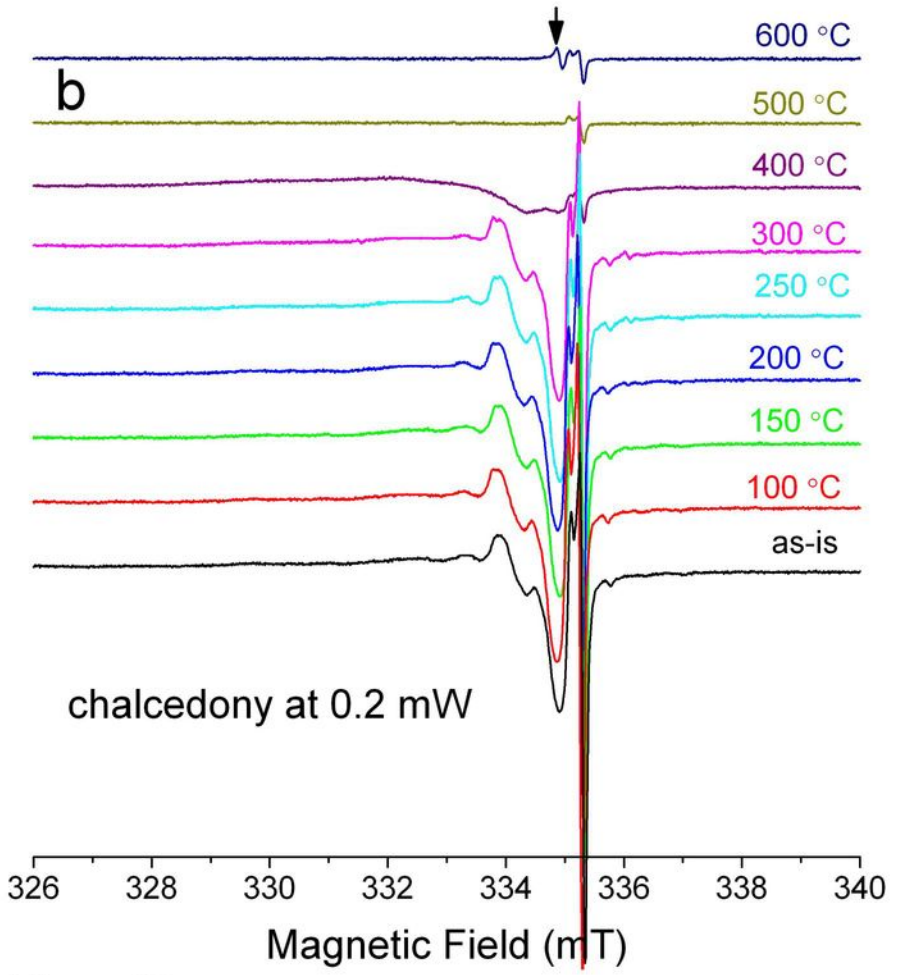
b
600 °C
500 °C
400 °C
300 °C
250 °C
200 °C
150 °C
100 °C
as-is
chalcedony at 0.2 mW
326
328
330
332
334
336
338
340
Magnetic Field (mT)

Figure 10

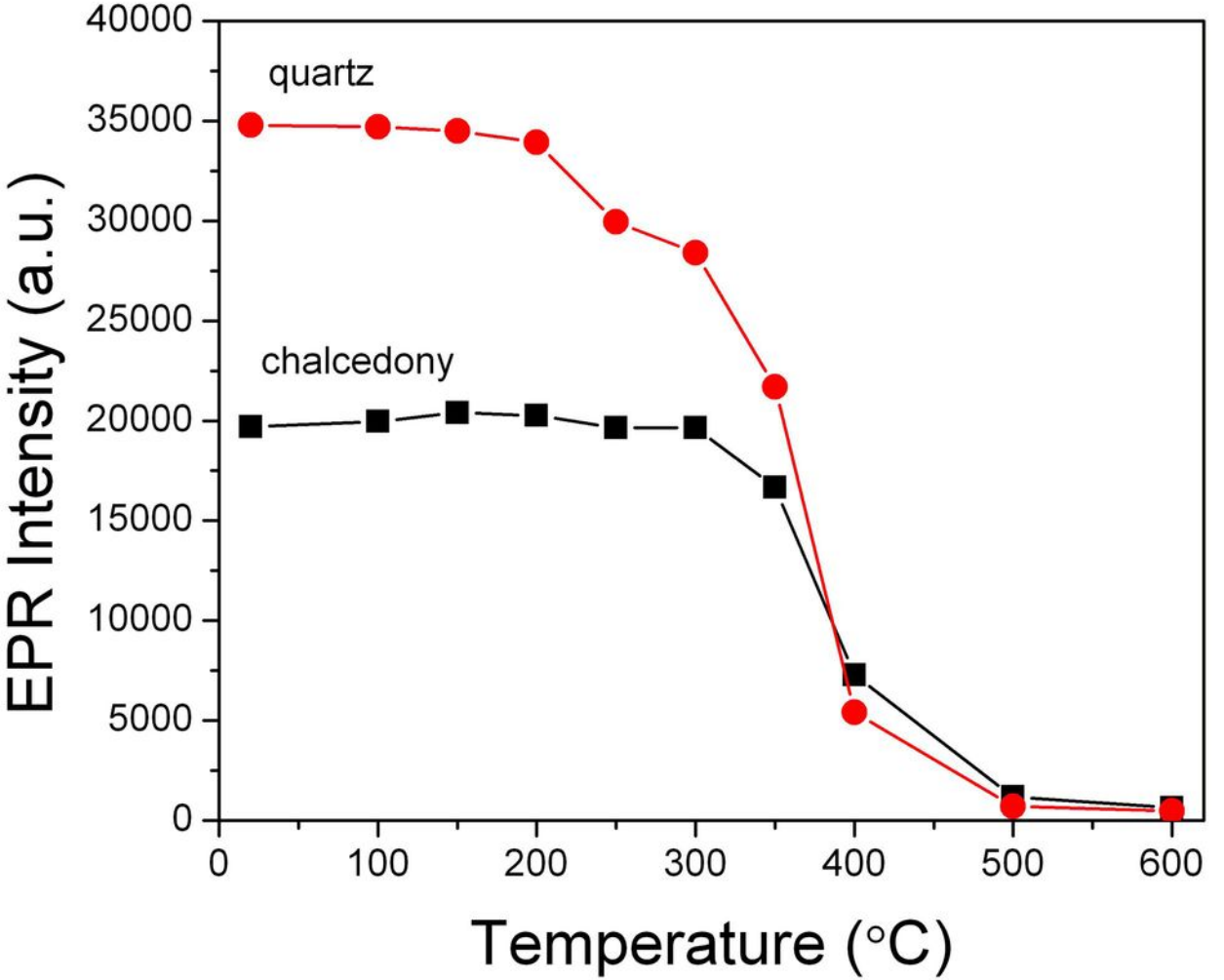
quartz
chalcedony
EPR Intensity (a.u.)
Temperature (°C)
0
5000
10000
15000
20000
25000
30000
35000
40000
0
100
200
300
400
500
600

Figure 11

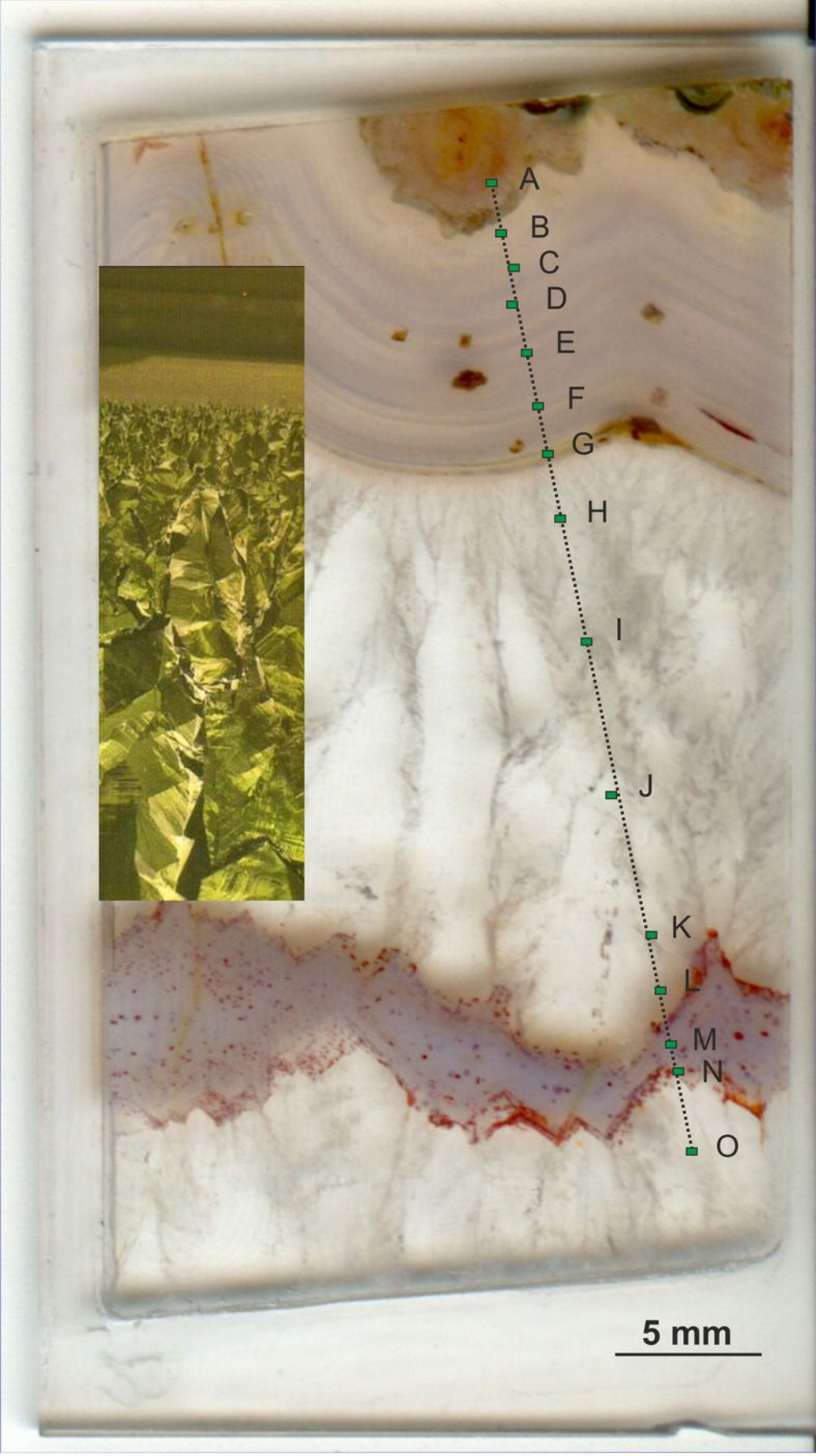

Figure 12

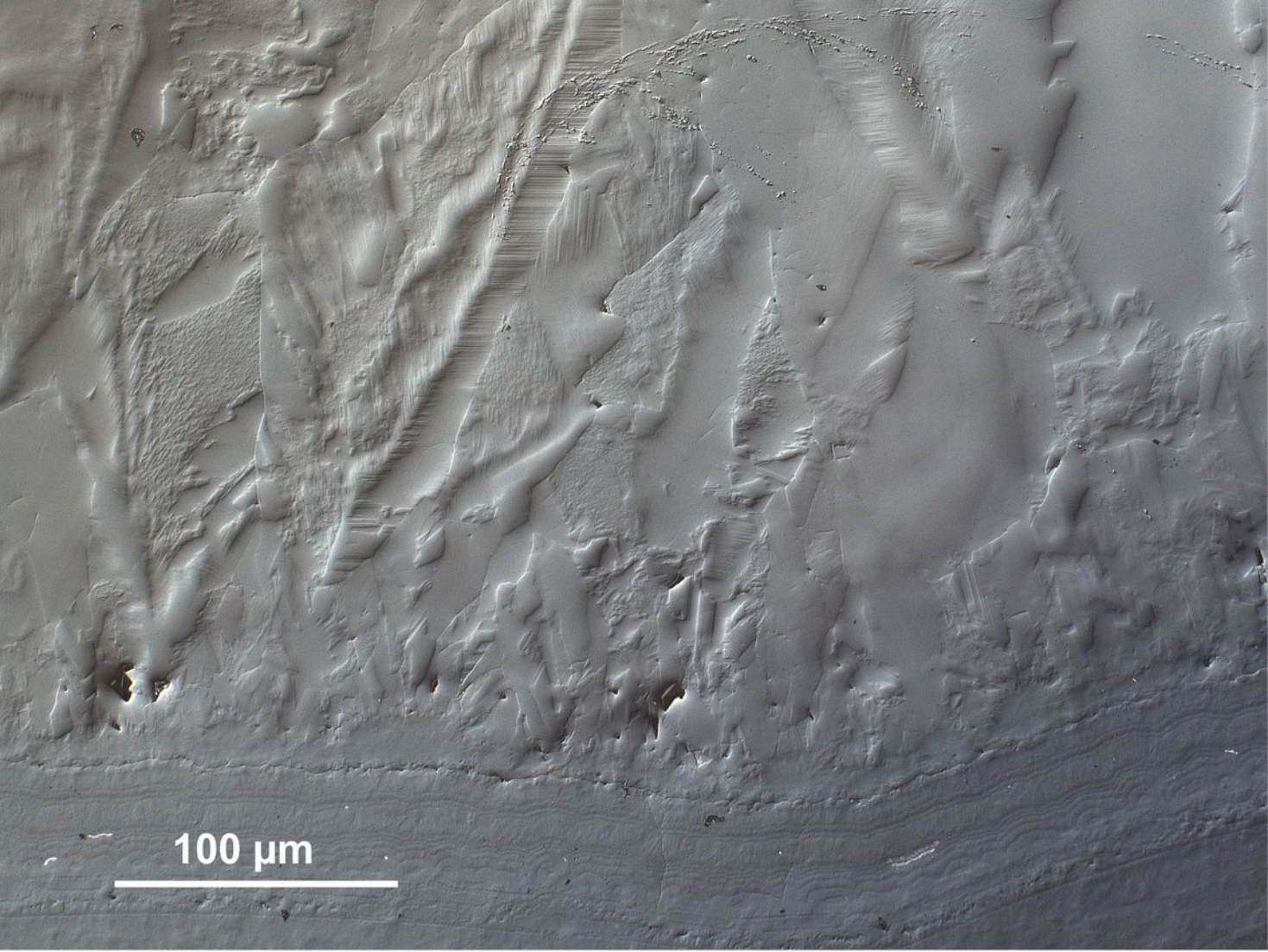

Figure 13